

**MULTIDISCIPLINARY INVESTIGATION OF C-TYPE COMPOSITE
SANDWICH RADOME PANELS WITHIN THE SCOPE OF ACOUSTIC
EMISSION BASED DAMAGE CHARACTERIZATION AND
ELECTROMAGNETIC TRANSMISSION PERFORMANCE**

By

Fatih UZUN

Submitted to the Graduate School of Engineering and Natural Sciences
in partial fulfillment of the requirements for the degree of
Master of Science

SABANCI UNIVERSITY

December 2020

MULTIDISCIPLINARY INVESTIGATION OF C-TYPE COMPOSITE SANDWICH RADOME PANELS WITHIN THE SCOPE OF ACOUSTIC EMISSION BASED DAMAGE CHARACTERIZATION AND ELECTROMAGNETIC TRANSMISSION PERFORMANCE

APPROVED BY:

[Redacted]

DATE OF APPROVAL: 25/12/2020

© Fatih UZUN 2020

All Rights Reserved

ABSTRACT

MULTIDISCIPLINARY INVESTIGATION OF C-TYPE COMPOSITE SANDWICH RADOME PANELS WITHIN THE SCOPE OF ACOUSTIC EMISSION BASED DAMAGE CHARACTERIZATION AND ELECTROMAGNETIC TRANSMISSION PERFORMANCE

Fatih UZUN

Manufacturing Engineering MSc. Dissertation, December 2020

Thesis Supervisor: Assist. Prof. Dr. Murat BUYUK

Thesis Co-Advisor: Prof. Dr. Mehmet YILDIZ

Keywords: Radome, BVID, K-Means Clustering, Sandwich Panel, Acoustic Emission, Free Space Test, Indentation Test, Scanning Electron Microscopy

This study aims to investigate the electromagnetic transmission performance of composite radome sandwich panel structures used in aviation and to cluster the damage mechanisms caused by barely visible impact damages within the panels with the Acoustic Emission (AE) method. Two different sandwich radome panel samples consisting of skin materials made of E-glass and aramid prepregs and Nomex® honeycomb as the core material are examined in the research. Flat sandwich panels with equal skin and core thicknesses are produced by the hot-press curing method.

Measurements of the electromagnetic transmission and reflection coefficients are performed by the free space test method in the frequency range of 5-25 GHz. As a result, transmission coefficients including dielectric coefficient and loss tangent values of the panel and its constituents are obtained experimentally. Sandwich panels are numerically

modeled as a multilayer substrate by using Hyperworks® FEKO software, where the material parameters that are obtained from the experimental study are used as the input for the model. Planar Green's function approach is used as the solver for the electromagnetic simulations and it is found that the results correspond well with the experiments. As a result, the aramid sandwich panel sample is showed better electromagnetic properties compared to the E-glass sandwich panel sample within the specified frequency range.

Barely Visible Impact Damage (BVID) characteristics are investigated in the samples with the quasi-static indentation test approach and the data obtained by the acoustic emission sensors are subsequently clustered with the k-means algorithm to examine and categorize the damage mechanisms that occur in the structure. *GAP* function is used to specify the optimum initial clustering value of the k-means algorithm. Aramid sandwich panel sample is deformed under the indentation loading and several different damage mechanisms are observed throughout the sample like matrix cracking, fiber breakage, and core crushing. Unlike the aramid samples, debonding and delamination are observed at the interface of the prepreg and core structure within the E-glass sandwich panel sample. Different failure and damage mechanisms within the microstructure are also verified by SEM images. Finally, it has been found that the acoustic emission method can be a useful approach in the damage classification of radome sandwich panels under quasi-static indentation loading. Besides, aramid sandwich panel can be a more suitable material for radome applications in high frequency operating conditions due to its low transmission losses and high structural strength against indentation loads.

Özet

AKUSTİK EMİSYON ESASLI HASAR KARAKTERİZASYONU VE ELEKTROMANYETİK İLETİM PERFORMANSI KAPSAMINDA C-TİPİ KOMPOZİT SANDVIÇ RADOM PANELLERİNİN ÇOK DİSİPLİNLİ ARAŞTIRILMASI

Fatih UZUN

Üretim Mühendisliği, Yüksek Lisans Savunması, Aralık 2020

Tez Danışmanı: Dr. Öğr. Üyesi Murat BUYUK

Tez İkinci Danışmanı: Prof. Dr. Mehmet YILDIZ

Anahtar Kelimeler: Radom, BVID, K-ortalamları Kümelendirmesi, Sandviç Panel, Akustik Emisyon, Boş Alan Testi, Girinti Testi, Taramalı Elektron Mikroskobu

Bu çalışmanın amacı, havacılıkta kullanılan kompozit radom sandviç yapılarının elektromanyetik iletim performanslarını incelemek ve neredeyse görünür darbe hasarlarının paneller içerisinde neden olduğu hasar mekanizmalarını Akustik Emisyon yöntemi ile (AE) kümelemektir. E-cam ve aramid reçine emdirilmiş kumaşlardan yapılmış yüzey katmanlarından ve çekirdek malzeme olarak Nomex® altıgen petekten oluşan iki farklı sandviç panel numunesi incelendi. Eşit yüzey ve çekirdek kalınlıklarına sahip düz şekilli sandviç paneller sıcak pres kütleme yöntemi ile üretilmiştir.

Elektromanyetik iletim ve yansıma katsayılarının ölçümü, 5-25 GHz frekans aralığında boş alan testleri ile gerçekleştirilmiştir. Panel ve bileşenlerinin dielektrik

katsayısı ve kayıp tanjant deęerlerini ieren iletim katsayıları deneysel olarak elde edilmiřtir. Sandvi paneller, Hyperworks® FEKO yazılımı kullanılarak ok katmanlı bir tabaka řeklinde sayısal olarak modellendi ve özdür yöntemi olarak Planar Green'in fonksiyonu yaklaşımı kullanılmıřtır. Boř alan testlerinden elde edilen elektriksel malzeme parametreleri sayısal model iin girdi olarak kullanılmıřtır. Elektromanyetik simülasyon ıktıları deneylerle mükemmel bir řekilde örtüřtüęü görülmüřtür. Sonu olarak, aramid sandvi panel numunesi, belirtilen frekans aralıęında E-cam sandvi panel numunesine kıyasla üstün elektromanyetik özelliklerle sahip olarak davranmaktadır.

Neredeyse Görünür Darbe Hasarları (BVID) yarı statik girinti testi yaklaşımı ile numunelerde incelenmiř ve akustik emisyon sensörlerinden elde edilen veriler daha sonra panellerde meydana gelen hasar mekanizmalarını sınıflandırmak iin k-ortalamları algoritması ile kümelendi. Akustik emisyon veri noktalarının optimum küme sayısını belirlemek iin *GAP* fonksiyonu kullanılmıřtır. Aramid sandvi panel numunesi girinti yüklemesi altında deforme olmuřtur ve numune boyunca matris atlamařı, elyaf kırılmařı ve ekirdek ezilmesi gibi birak farklı hasar mekanizması gözlemlenmiřtir. Aramid numunelerinden farklı olarak, E-cam sandvi panel numunesindeki üst tabaka ve ekirdek yapısının arayüzünde baę ayrılmařı ve delaminasyon gözlenir. Panellerin mikroyapısında AE ile elde edilen hasar tipleri, kırık yüzeylerin Taramalı Elektron Mikroskopu (SEM) alıřmaları ile doęrulanmaktadır. Son olarak, akustik emisyon yönteminin yarı-statik girinti yüklemesi altında radom sandvi panellerin hasar sınıflandırmada faydalı bir yaklaşım olabileceęi bulunmuřtur. Ayrıca aramid sandvi panel, düşük iletim kayıpları ve girinti yüklerine karřı yüksek yapısal mukavemeti nedeniyle yüksek frekanslı alıřma kořullarında radom uygulamaları iin daha uygun bir malzeme olabilir.

Acknowledgment

First, I would like to thank the Dean's Office of Faculty of Engineering and Natural Sciences for their financial support to conduct my study at Sabancı University which is one of the most distinguished universities in Turkey. Afterward, I would like to present my appreciation to my thesis advisors professors Mehmet Yıldız and Murat Buyuk for their support throughout my research. I think that it would be impossible for me to complete my master's degree without their assistance.

Next, I want to express my gratitude to Dr. Isa Emami Tabrizi, Mr. Hafiz Qasim Ali, and Dr. Çağatay Yılmaz for their contribution and help during the research work. After that, I would like to acknowledge Mr. Çağhan Tuncer and all the members of the Sabancı Motorsport Formula Student Team for their continuous motivation and loyalty. Finally, I would like to thank all the technical staff of SUIMC and Kordsa for their help in the production and testing stages of my study.

Table of Contents

ABSTRACT	iv
Özet	vi
Acknowledgment	viii
CHAPTER 1	1
1. Outline of the Thesis	1
CHAPTER 2	2
2. Literature Review	2
2.1 Definitions	2
2.2 History and Background	6
2.3 Problem Description	8
2.4 Dielectric Theory	10
2.5 Free Space Method Electromagnetic Test	13
2.6 Fiber Reinforced Polymeric Composites	15
2.7 Honeycomb Sandwich Structures	19
2.8 Scanning Electron Microscopy (SEM)	23
2.9 Planar Green's Function Approach	25
2.10 Quasi-static Indentation Tests	26
2.11 Acoustic Emission (AE)	27
CHAPTER 3	34
3. Electromagnetic Transmission Performance of Radome Sandwich Panels	34
3.1 Experimental	35
3.2 Experimental Test Setup	40
3.3 Electromagnetic Simulation	41
3.4 Results and Discussions	44
CHAPTER 4	48
4. Damage Characterization of Radome Sandwich Panels	48
4.1 Materials and Manufacturing of Sandwich Panels	48
4.2 Experimental Test Setup	48
4.3 Quasi-Static Test Results and Discussion	50
4.4 Acoustic Emission Results and Clustering	52
4.5 Scanning Electron Microscopy Analysis of Failed Sandwich Panels	62
CHAPTER 5	66
5. Conclusion	66
References	68

List of Figures

Figure 1. Radome sandwich panel configurations	3
Figure 2. Photograph of a B-18A aircraft. [2]	7
Figure 3. Radome-enclosed missile guidance antenna. (Photo courtesy of USAF National Museum.) [2]	8
Figure 4. Parallel plate capacitor, DC case [6]	10
Figure 5. Parallel plate capacitor, AC case [6]	11
Figure 6. Free-space electromagnetic test setup with dual horn antennas [10]	14
Figure 7. Composition of a composite plate with a chopped fiber content [67]	15
Figure 8. Thermoplastic polymer chains, b- Cross-link bonds [68]	16
Figure 9. Matrix types and subcategories [69]	17
Figure 10. Heterogenous isotropy/anisotropy, Homogenous isotropy/anisotropy [70]	19
Figure 11. Schematic of a honeycomb sandwich panel with its main components [71]	19
Figure 12. Side to side schematics of a sandwich panel and an I-beam. [72]	20
Figure 13. Sandwich panel under load. Load is carried by the face sheets and core structure is in shearing. [73]	21
Figure 14. Sandwich panel stiffness, flexural strength, and weight for various core thicknesses [74]	21
Figure 15. Various core structure cell types. [22]	22
Figure 16. Leo SUPRA 35VP FEG-SEM measurement device [75]	24
Figure 17. Radiofrequency wave acting on a spherical shape radome with specified incident angles and assumption of locally tangent planar structure [26]	25
Figure 18. Radome panel multilayered medium in terms of Planar Green's theorem [26]	26
Figure 19. Schematic of acoustic emission testing and PZT transducer [76]	30
Figure 20. Acoustic emission hit based waveform features [77]	32
Figure 21. Electromagnetic performance assessment research steps	34
Figure 22. Schematic representation of the hot press curing process and layer layout [78]	36
Figure 23. Waterjet cutting free space test specimen preparation.	37
Figure 24. Aramid skin and honeycomb core radome sandwich panel free space test specimen	37
Figure 25. Aramid laminate free space test specimen	38
Figure 26. E-glass laminate free space test specimen	38
Figure 27. E-glass skin and honeycomb core radome sandwich panel free space test specimen	39

Figure 28. Aramid and E-Glass honeycomb panel hot press layup	39
Figure 29. Free space test setup [79].....	40
Figure 30. Vector network analyzer components diagram [10].....	41
Figure 31. Electromagnetic transmission simulation radome sandwich panel model.....	43
Figure 32. Electromagnetic transmission simulation E-Glass radome sandwich panel model multilayer substrate parameters.....	43
Figure 33. Electromagnetic transmission simulation Aramid radome sandwich panel model multilayer substrate parameters.....	43
Figure 34. Free space test dielectric constant results	44
Figure 35. Free space test loss tangent results.....	45
Figure 36. Comparison of free space test and electromagnetic simulation transmission loss results	46
Figure 37. Comparison of free space test and electromagnetic simulation reflection loss results of the specimens.....	47
Figure 38. Mistras Acoustic Emission Test Setup	49
Figure 39. Piezo electric acoustic emission sensors placement on the specimens: a) Aramid sandwich panel, b) E-Glass sandwich panel	50
Figure 40. Quasi-static indentation test load and deflection results.....	51
Figure 41. Aramid sandwich panel before (a) and after (b) the indentation test.....	52
Figure 42. E-glass sandwich panel before (a) and after (b) the indentation test.	52
Figure 43. AE Counts versus Weighted Peak Frequency plot of Aramid and E-Glass Samples	53
Figure 44. Aramid panel GAP values of calculated for each cluster.	54
Figure 45. E-Glass panel GAP values of calculated for each cluster.....	55
Figure 46. Acoustic emission vs Weighted Peak Frequency graph of aramid panels in terms of k-means algorithm clusters.	56
Figure 47. The variation of cumulative AE energy and load as a function of time for the aramid panel.....	58
Figure 48. Acoustic emission vs Weighted Peak Frequency graph of E-Glass panels in terms of k-means algorithm clusters.	59
Figure 49. Cumulative AE Energy versus Load chart of E-Glass panel in time domain.....	60
Figure 50. Damage types observed in the face sheet of the E-glass panel.....	62
Figure 51. Micrograph of the fiber-pull out damage mechanism observed in the face sheet of the E-glass panel.	63
Figure 52. SEM image of the delamination damage mechanism between E-glass face sheet layers	64

Figure 53. Various face sheet and honeycomb core damage mechanisms existing on the interface of the E-glass panel.	64
Figure 54. Damage mechanisms of the aramid panel in the microstructure	65

List of Tables

Table 1. Material properties and units of the radome material in terms of functions.....	5
Table 2. Composite skin materials in radome applications: resin system and fiber reinforcement	6
Table 3. Detailed information and properties of radome sandwich panel face sheet plies.....	35
Table 4. Electromagnetic transmission simulation input parameters	42

List of Equations

$C_0 = \frac{A}{t}$	Equation1.....	10
$C = C_0\kappa'$	Equation2.....	10
$\kappa' = \varepsilon'_r = \frac{C}{C_0}$	Equation3.....	10
$I = I_c + I_l = V (j\omega C_0\kappa' + G)$	Equation4.....	11
$G = \omega C_0\kappa''$,	Equation5.....	11
$I = V (j\omega C_0) (\kappa' - j\kappa'') = V(j\omega C_0) \kappa$	Equation6.....	11
$\omega = 2\pi f$	Equation7.....	11
$\kappa = \kappa^* = \varepsilon_r = \varepsilon_r^*$	Equation8.....	12
$D_f = \varepsilon E$	Equation9.....	12
$\varepsilon = \varepsilon^* = \varepsilon_r \varepsilon_0$	Equation10.....	12
$\varepsilon_0 = \frac{1}{36\pi} \times 10^{-9} \text{ F/m}$	Equation11.....	12
$\kappa = \frac{\varepsilon}{\varepsilon_0} = \varepsilon_r = \varepsilon_r - j\varepsilon_r''$	Equation12.....	12
$L = L_w + L_B$	Equation13.....	13
$CPT = \left(\frac{n \times W}{1000 \times \rho_f \times \rho_m} \right) \times \left[\frac{\rho_f}{W_f} - (\rho_f - \rho_m) \right]$	Equation14.....	36
$W_f = \frac{\rho_f \times V_f}{\rho_f \times V_f + \rho_m \times V_m}$	Equation15.....	37
$f_{centroid} = \frac{\sum_{s=0}^{s=100} f(s)M(s)}{\sum_{s=0}^{s=100} M(s)}$	Equation16.....	54
$WPF = \sqrt{f_{centroid} \times f_{peak}}$	Equation17.....	55
$GAP_n(k) = E_n^*\{\log(\omega_k)\} - \log(\omega_k)$	Equation18.....	55

CHAPTER 1

1. Outline of the Thesis

- Chapter 2: Provide details about the history and background of the radome types and materials. Next, explains the problem description and main focus items of the thesis. Fundamental equations and the terms that are related to the dielectric theory are mentioned. The free space test method and the literature findings of this method are given. Technical explanations and related studies about the methods which are used in the rest of this research such as acoustic emission and scanning electron microscopy.
- Chapter 3: provides detailed information about electromagnetic compatibility simulations and experimental research. The production method and the parameters that are related to sample dimensions are given. Key parameters such as sample physical properties, the frequency band of the tests. Assessments of the electromagnetic research steps. Results and discussions about the transmission and reflection loss of the samples.
- Chapter 4: It contains information about the acoustic emission test setup and techniques used during measurement. Interpretation of quasi-static test results. How the acoustic emission data are clustered with the k-means algorithm and damage criteria are defined. Comparison of aramid and e-glass sandwich panels in terms of structure
- Chapter 5: concludes the research with a comparison of samples in terms of an ideal radome material requirements by synthesizing the electromagnetic and structural test and analysis results. To explain the suitability and adequacy of the methods used in the research.

CHAPTER 2

2. Literature Review

2.1 Definitions

A radome is a protective structure that acts as an electromagnetic window and is developed to ensure that antennas and similar structures are not affected by environmental conditions and protected against damage. The word “Radome” is derived from the combination of the words “radar” and “dome”. For the radomes to operate in a proper way, they must concurrently be designed to withstand some of the structural loads such as bird strike, runway debris, hail strike, and aero-related loads. They must also transmit radio frequency (RF) waves with a minimal loss under operational conditions. Generally, it is necessary to make a smart trade-off between electromagnetic and mechanical design parameters when designing a radome that serves the desired performance and purpose. The electromagnetic performance of an antenna protected with a radome structure is always affected due to interaction between the radome material's interface and the electromagnetic field. Parameters such as amplitude, phase, and polarization changes, and the near electromagnetic field of the antenna causes distortion [1]. One of the most important factors in radome design is the environmental conditions and it also affects the type of material, wall type, and radome shape. All radome designs should be made by considering the structural loads, operating temperatures, parameters such as vibration, humidity, and rain.

Radomes are classified by the MIL-R-7705B standard according to the platforms in which they are used and details of their wall designs [2]. Radomes are classified according to their general purpose of use and the platform in which they are used; as Class I (flight vehicles), Class II (surface vehicles) and, Class III (fixed ground installations). Radomes are also classified into five basic groups according to dielectric wall design types and configurations as illustrated in Figure 1 and the details can be listed as:

- A-Type radomes are called monolithic half-wave wall structures.
- B-Type radomes are also monolithic structures but in this type of radomes, wall thickness is thinner than A-Type radomes and it has a thickness less than 0.1λ (wavelength) or less than this value.
- C-Type radomes have a sandwich panel structure and are also called a-sandwich multi-layer wall. There are two high-density face sheets in the panel design with a lower density core materials in between. The dielectric constant of the core material is lower than the skin material's dielectric constant.
- D-Type radomes are very similar to C-Type radomes in terms of construction. They consist of high-density skin and low-density core material. They contain five or more skin layers and consist of more than two core materials. By increasing the number of layers, it is ensured to operate at broadband frequency.
- E-Type covers all remaining radome types. B-sandwich radome structures are in this class. Unlike A-type radome sandwiches, they are composed of low-density skin and high-density core material. The dielectric coefficient of the core material is greater than skin material.

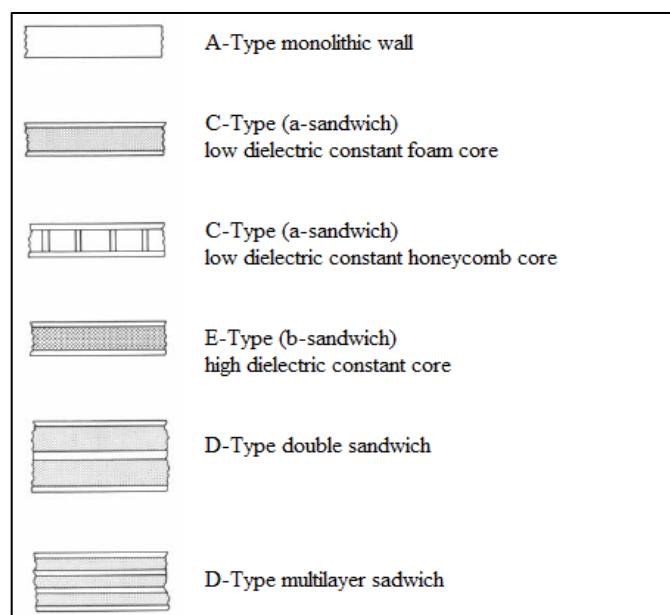


Figure 1. Radome sandwich panel configurations.

Considering that C-Type a-sandwich radomes are used in aviation applications, various parameters of this type possess importance with the material selection.

A-sandwich radomes usually have a core material that has a low density and low dielectric coefficient between the skins with high dielectric coefficient and density. In a-sandwiches used in aviation applications, fiberglass is often chosen as the skin material and phenolic honeycombs are often preferred as the core material [2]. The thickness of the skins is often chosen as 0.75 mm or more to provide the necessary structural strength. An a-sandwich wall design is good in strength to weight ratio, also has good electrical performance at low incidence angles.

One of the most important requirements of an ideal radome material is being electrically highly transparent and providing the minimum transmission loss during the passage of electromagnetic waves through the wall [3]. It is expected to be durable in terms of strength throughout the flight lifetime of the part by maintaining its physical integrity under aerodynamic loads, environmental conditions, and thermal loads. An ideal radome material should also behave like ambient covering all electromagnetic wavelengths in terms of electrical properties. While choosing the radome material, it is a critical step to make the most suitable design trade-off between the material parameters according to the desired application conditions.

Considering the electrical performance, the targeted properties that affect the radome material are smaller values of transmission loss during electromagnetic wave radiation, which are dielectric coefficient and loss tangent. For the radome structure to have a suitable design in terms of construction throughout its operating life, parameters such as strength, density, and durability of the material are important considering the mechanical loads. For the radome material to behave stable under thermal conditions, thermal conductivity, emissivity, thermal shock, and temperature changes are the parameters that should be considered during the design phase. When the production processes and methods are evaluated, environmental conditions and factors that will create contamination should be avoided in order not to degrade the radome material.

For instance, a material with a low dielectric coefficient can be selected for radome structures that will operate in a wide frequency band, while a material with a high

dielectric coefficient can be selected for a narrower frequency band and minimum aberration. Therefore, glass and aramid fiber-reinforced polymer sandwich structures and composites in solid laminate forms stand out. General material properties of radome structures are listed in Table 1:

Table 1. Material properties of radome structures.

Function	Property	Unit
Electrical	Dielectric constant	-
	Loss tangent	-
	Volume resistivity	ohm cm
	Dielectric strength	kv/mm
Mechanical	Specific gravity	-
	Density	g/cm ³
	Stress and Elastic Moduli	N/m ²
	Poisson's ratio	-
	Viscosity	Poise
Thermal	Specific heat	cal/kg °C
	Thermal conductivity	cal/cm s °C
	Diffusivity	cm ² /s
	Emissivity	-
	Thermal expansion	per °C
	Temperature	°C
	Radiation	Rads

The materials that are chosen in today's radome technology are combinations of layered composites such as E-glass, D-glass, aramid, quartz coupled with resin (matrix) systems such as epoxy, polyester, polycyanete [1]. Foams and honeycomb structures are generally preferred as the core material of the sandwich panels since they provide, low

dielectric coefficients and increase the electromagnetic wave transmission performance of the radome while increasing the stiffness in structural terms. Common radome reinforcement and relevant resin types are given in Table 2.

Table 2. Composite skin materials in radome applications with relevant resin system and fiber reinforcement.

Reinforcement	Resin
E-glass	Epoxy
	Polyester
	Polyimide
D-Glass	Polycyanate
Polyethylene	Epoxy
	Polyester
	Polycyanate
Kevlar	Polyester
Quartz	Epoxy
	Polyester
	Polyimide
	Polycyanate
	Polybutadiene
	Bismaleimide

2.2 History and Background

With the “Very High Frequency” radar mounted on slow-speed aircrafts that are used during the II World War, the need for the development of a radome that will protect the antennas during the flight has emerged [2]. During 1940s, the need for the protection of radars has increased because of the use of microwave radars. A photograph of a B-18A aircraft with such a radome is shown in Figure 2. Due to the high-performance demand, the radomes had to be designed to provide more precise transmission tolerances at larger

scales and short wavelengths [57]. In 1941, the first radome that was used in a real flight was a thin-walled structure and its material was made of plexiglass. This radome, which had a geometrically hemispherical structure, was like today's airborne radomes in terms of construction. Plywood material was preferred for the radomes used in the early 1943's and they had a thickness of approximately 0.25 inches [4]. During these years, radomes made of plywood material were used in blimps and boats in the U.S. army, where, moisture absorption was a significant problem. Moreover, alternative materials were investigated since plywood was not a compatible material with curved geometries.



Figure 2. Photograph of a B-18A aircraft [2].

As a result of the studies carried out by the MIT Radiation Laboratory in 1944, the first a-sandwich form consisting of 3 layers was developed. High-density fiberglass was preferred for the skins of the sandwich panel, while a combination of polystyrene fiber with lower density was used for the core material [5].

Since the World War II, the development of radomes have continued in two different areas of the material of choice. While radome structures with ceramic materials are preferred primarily in hyper-velocity missiles due to heating, composite sandwich panels are preferred in areas requiring high strength. The modern radomes that are used today

has a composite sandwich panel structure. A radome with a nose-shape that is constructed with a composite sandwich panel structure is shown in Figure 3.

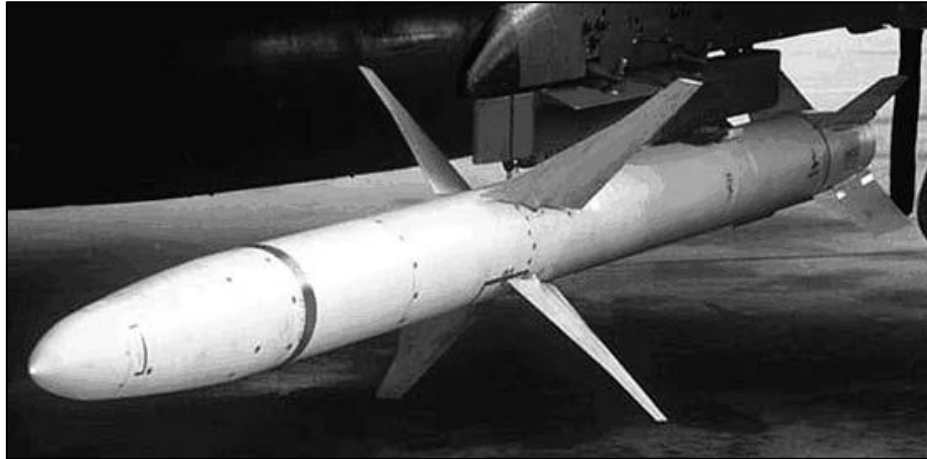


Figure 3. Radome-enclosed missile guidance antenna. (Photo courtesy of USAF National Museum.)[2].

Computerized calculations and analysis methods have evolved to meet the electromagnetic performance criteria required for new avionics and radars. The fact that the parameters required for the design and analysis phase necessitate an interdisciplinary study, which is essential to utilize computerized calculation techniques.

2.3 Problem Description

Designs consisting of composite sandwich panels constitute a large share of the market of radomes used in areas such as aviation, defense, and maritime. Panels are generally used in the form of a C-type sandwich consisting of thin shells surrounding a thick core material. Radomes are used for the protection of antennas used in communication and radar applications operating in different frequency ranges. Radome design consists of many stages from concept to final product stage such as material characterization, production management, mechanical and electromagnetic requirements,

geometric shape design. The focus of the research in this thesis is the studies on the material-based characterization stage.

The dielectric coefficient and loss tangent values are important in terms of electromagnetic performance when choosing the suitable materials that make up the radome structure. These parameters change depending on the frequency. X, Ku, and K bandwidths have been chosen as the frequency range in which the radome will operate. While making this choice, the frequency operating range of the antennas used in today's modern aviation vehicles and generally located in the nose and fuselage structure of the vehicle is considered. In this frequency band, the dielectric coefficient and loss tangent values should be as low as possible for the radome to show the desired electromagnetic performance and to have low transmission loss coefficients. In this way, electromagnetic waves reach the antennas by passing through the radome wall with the least amount of loss. It is aimed that the radome structure will serve as an insulating window between the environment and antennas. The problem here is that in addition to the electromagnetic characteristics of the radome, it should also provide the structural integrity of the system by protecting the antenna structure mechanically from barely visible impact damage such as aerodynamics loads, bird strikes, runway debris strikes, and tool drops during maintenance. This type of damage is called barely visible impact damage because the radome structures are mostly composed of composite materials, and although the mechanical damages that will occur because of impacts at low speeds do not show significant damage from the surface due to the composite material, damage mechanisms such as fiber breakage, delamination, debonding and core crushing can occur. The results obtained by performing quasi-static indentation tests based on samples will be demonstrated with the data obtained from acoustic emission sensors to detect such damages in composite sandwich panels and to examine at what loading condition values they occur. E-glass and aramid composite flat radome samples selected at the end of experimental and computational studies are compared in terms of electromagnetic and mechanical performances.

2.4 Dielectric Theory

When an external electric field is applied, materials with energy storage capability are classified as “dielectric”. When a dielectric material is placed between two plates parallel to each other and DC voltage is applied, more charge can be stored compared to the absence of any material (a vacuum) between the two plates. In case a dielectric material is used, neutralizing charges on the electrodes contributes to an increase of the energy storage capacities of the capacitors. As mentioned above, there is a connection between capacitance with a dielectric material and the dielectric coefficient. The parallel plate capacitor AC schematic is given in Figure 5.

$$C_0 = \frac{A}{t} \quad (1)$$

$$C = C_0 \kappa' \quad (2)$$

$$\kappa' = \epsilon_r' = \frac{C}{C_0} \quad (3)$$

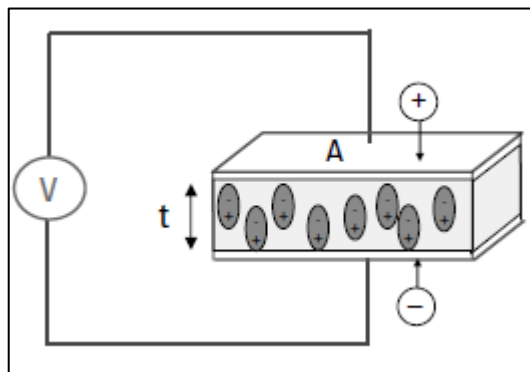


Figure 4. Parallel plate capacitor, DC case [6].

C and C_0 refer to capacitance with and without dielectric as given in Equation 1 and 2, $\kappa' = \epsilon_r'$ is the permittivity or dielectric constant as shown in Equation 3, A and t are the geometrical dimensions of the capacitor plates (Figure 4.). If an AC sinusoidal voltage is applied to the same capacitor at this time, two parameters named charging current I_c and loss current I_l will be formed in the resulting current as given in Equation 4 and that is related to the dielectric constant. The losses in the material with a parallel capacitor (C) are called conductance (G) as stated in Equation 5.

$$I = I_c + I_l = V(j\omega C_0 \kappa' + G) \quad (4)$$

$$\text{If } G = \omega C_0 \kappa'', \text{ then} \quad (5)$$

$$I = V(j\omega C_0)(\kappa' - j\kappa'') = V(j\omega C_0) \kappa \quad (6)$$

$$\omega = 2\pi f \quad (7)$$

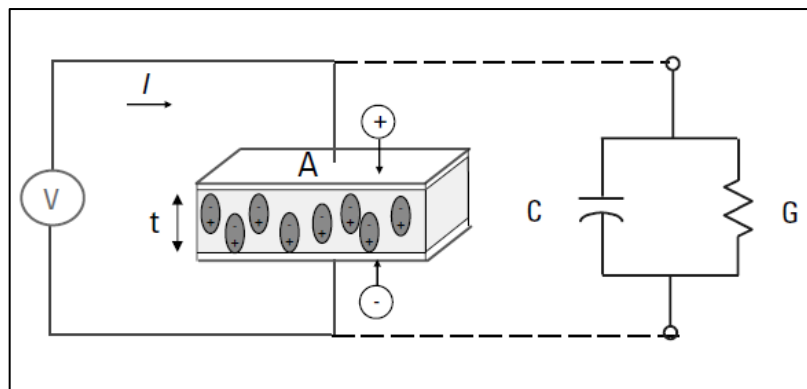


Figure 5. Parallel plate capacitor, AC case [6].

κ refers to complex dielectric constant as given in Equation 8 and it is the combination of two material electrical property as κ' indicates the real part and means storage, κ'' indicates the imaginary part and means loss.

The notation used in the literature for complex dielectric constant interchangeability is as follows:

$$\kappa = \kappa^* = \varepsilon_r = \varepsilon_r^* \quad (8)$$

In terms of electromagnetic theory, description of electric displacement (electric flux density) D_f is stated in Equation 9

$$D_f = \varepsilon E \quad (9)$$

Absolute permittivity ε consists of relative permittivity ε_r and free space permittivity ε_0 are shown in Equation 10 and 11

$$\varepsilon = \varepsilon^* = \varepsilon_r \varepsilon_0 \quad (10)$$

$$\varepsilon_0 = \frac{1}{36\pi} \times 10^{-9} \text{ F/m} \quad (11)$$

Permittivity is a complex quantity and is an electrical property of the material which describes its relationship to the electric field E as given in Equation 12

$$\kappa = \frac{\varepsilon}{\varepsilon_0} = \varepsilon_r = \varepsilon_r - j\varepsilon_r'' \quad (12)$$

We can evaluate the transmission losses of radomes by separating them into two main factors. These parameters are related to the frame structure of the radome and the material itself.

$$L = L_w + L_B \quad (13)$$

The two most important parameters when evaluating the electromagnetic performance while designing the radome are the permittivity and dielectric loss tangent values. When the dielectric constant and loss tangent values of the material are analyzed together with the wall thickness of the radome, the transmission and reflection coefficients formed in the radome wall are calculated. The radome system's signal scattering losses arising from the frame are expressed as given in Equation 13 with L_B . The value of the wall transmission loss arising from the radome material is expressed as insertion loss L_w and in many cases has less effect than the losses due to the frame structure. While evaluating the electromagnetic wave transmission performance of the material alone, the frequency-dependent insertion loss value should be analyzed.

2.5 Free Space Method Electromagnetic Test

It is important to characterize the radome structures in the form of sandwich panels that have become final products by applying them to electromagnetic tests and obtaining dielectric coefficients under different frequencies. If the final product radome structure has different geometric dimensions at wall thicknesses determined by the electromagnetic permeability tests performed at the beginning of the design cycle, it may cause shifts in the frequency band of the radome [6]. For use to measure the electromagnetic properties of the material in a predetermined frequency band, coaxial waveguide methods have been proposed by Baker-Jarvis et al. [7] and Tereschenko et al [8]. In these tests, the sample in the form of a sandwich panel is placed in a waveguide in the direction of the coincident axis, and then an electromagnetic wave is applied, then scattering parameters are obtained. The free space method, which enables to measure scattering parameters more

comprehensively and easily in large-sized samples, is proposed by Baker-Jarvis et al [7]. In past studies, the dielectric coefficient was obtained by making electromagnetic wave measurements of the material at a frequency of 30 GHz and above using the free space test method [9]. In recent years, with the developments in microwave network analyzers and the use of horn antennas that can provide better focus in the far-field, precise measurements can be made in the frequency bands in microwaves in the free-space method. The free-space test method has many advantages over the coaxial waveguide method. Measurements of dielectric coefficient with the free space method are a non-destructive method in terms of sample integrity. It is also ideal for high-temperature dielectric measurements as it does not require any contact on the sample. In the cavity waveguide method, because the sample is machined according to the cross-sectional areas of the waveguide, the sensitivity values during processing affect the accuracy of the measurement values of the sample. Since the electromagnetic waves emitted from the antennas during free-space measurements can be focused according to the position of the sample, there is no need to use a test fixture [10]. Figure 6. shows the measurement setup of a free-space method test with S-parameter configuration.

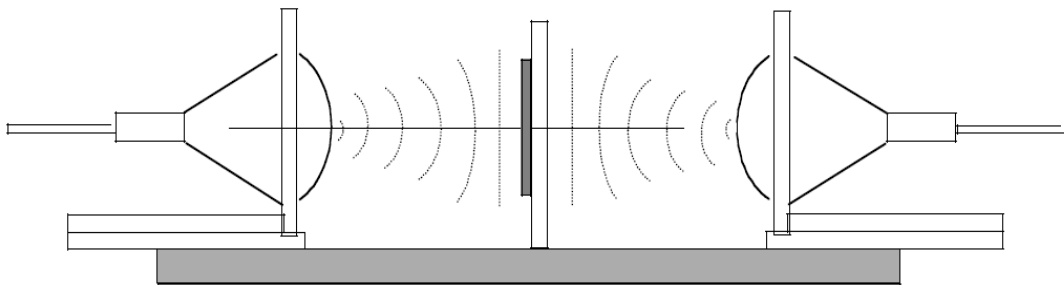


Figure 6. Free-space electromagnetic test setup with dual horn antennas [10].

2.6 Fiber Reinforced Polymeric Composites

Fiber-reinforced plastics are composite materials made up of two main parts. The fiber and the matrix. Matrix is a continuous and homogeneous medium where it binds and holds the fibers together. Fibers are continuous long strings with very low stiffness and high tensile strength.

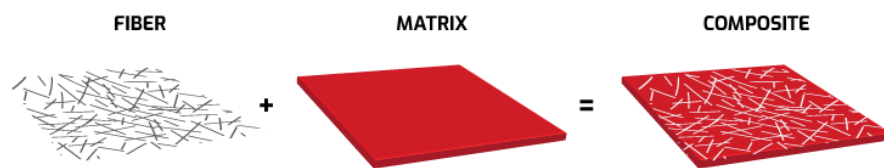


Figure 7. Composition of a composite plate with a chopped fiber content [67].

In FRP applications fibers can be selected from a wide range of materials such as carbon, glass, aramid, paper, basalt, etc. The polymer matrix is usually an epoxy resin, phenolic resin, vinyl ester, or polyester thermoset. Although the main selection factors are the structural properties, weight, and price of the material it is also important to consider ambient temperatures, humidity, and chemical contacts with the material [11].

In general, composite parts are a combination of two different materials with different mechanical and chemical properties as shown in Figure 7. The reason for the combination is to tailor-made a specific property material. Fiber-matrix combination can be altered to achieve specific mechanical and electrical properties such as dielectric properties, acoustic properties, or thermal properties [12].

Due to the ability to be tailor-made, FRP applications are used in advanced engineering applications, the aviation sector, military, and infrastructure where the weight to strength ratio is important.

One of the most common polymer matrixes is Thermoset resins. Most of the time these resins are in form of liquids before the curing process. They are turned into solid polymers by the process called polymerization. The polymerization process starts around the curing temperature and changes the chemical properties of the liquid resin by establishing cross-linked structures starting from the jellification stage until the curing completes. Due to the cross-linked polymers, the structure becomes completely solid and the process cannot be reversed back to the liquid stage after setting, hence called thermoset. Since thermoplastics cannot be reshaped due to the irreversibility of the process, they perform great in conditions with high heat and pressure without significantly losing its strength [13]. That is why thermoset plastics are mainly preferred by the aerospace industry. Overall thermoset materials are more resistant to solvents and corrosive environments. However, due to their thermoset properties, these polymers cannot be recycled. In some cases, it might be possible to recycle the thermoset polymer, but the energy required makes this process unfeasible. There is a new class of thermoset polymers that can be recycled, called polyhexahydrotriane's but due to the strong acids required to dissolve the thermoset, it is not a preferred material.

Thermoplastic polymers are plastic polymers that can be reshaped with a specific heat applied. Although the recyclability is not infinite, it can be recycled many times which makes thermoplastics more sustainable and ecofriendly. Ability to soften and reharden the material allows ease of manufacturing for complex geometries with techniques like thermoplastic welding, heat press molding, extrusion, and injection molding [14].

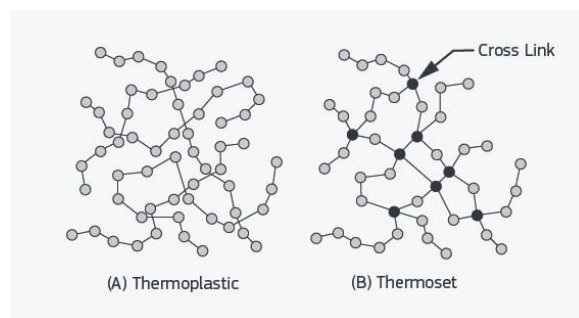


Figure 8. Thermoplastic polymer chains, b- Cross-link bonds [68].

Thermoplastic polymers have links of polymer chains that holds the monomers together as shown in Figure 8. When compared to thermoset polymers, thermoplastics have weaker intermolecular forces between the polymer chains. Since thermoplastics do not have cross-links between chains when heated energy required to break the polymer chain decreases making the material malleable.

Thermoset polymers have strong covalent type bonds between the polymer chains. Due to the cross-link between the chains, the material does not soften or changes chemical properties when heated. Main categories of matrix types are given in Figure 9.

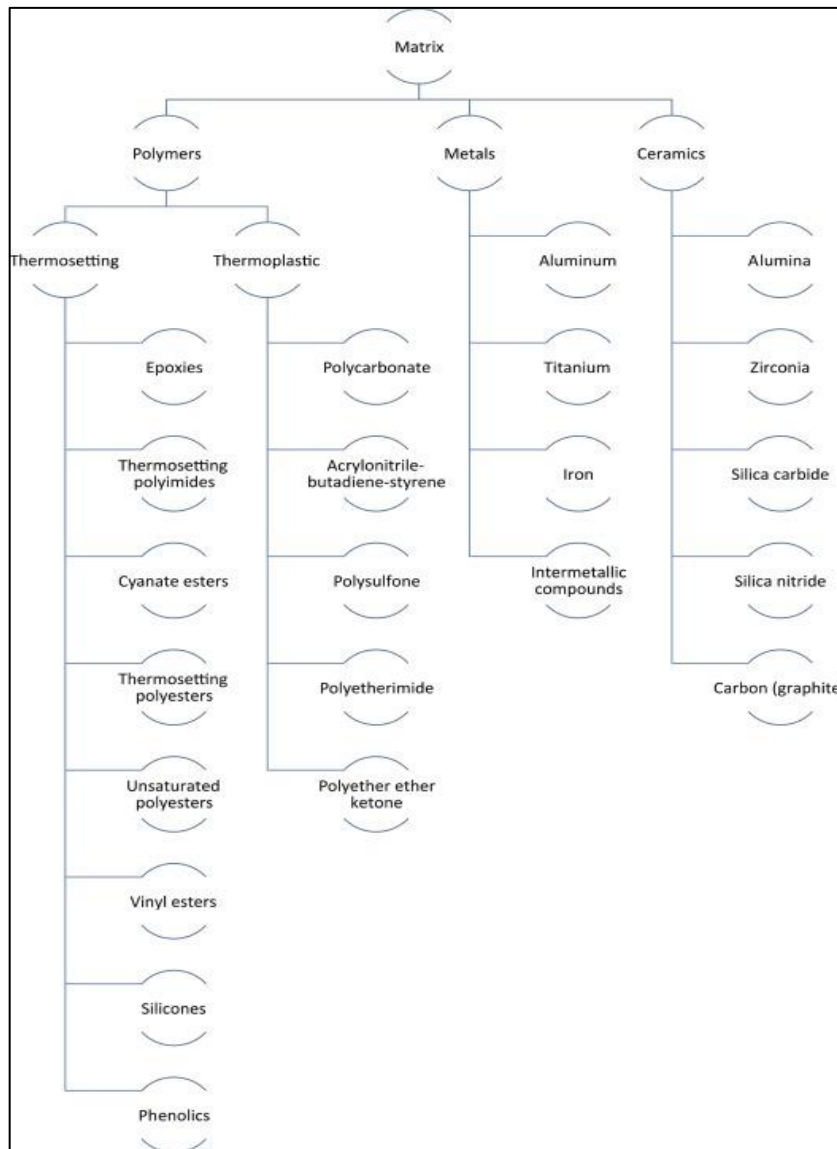


Figure 9. Matrix types and subcategories [69].

Fibers used in FRP applications can be organic or inorganic. These fibers are the main component of the composites that defines the structural properties. For high-performance applications, most of the time carbon, aramid or boron fibers are preferred [15]. Usually, these high-performance fibers are selected either because of their high tensile strength or their chemical properties [16].

Fabrics made from these fibers usually come in two main types: Unidirectional fabrics or woven fabrics. Unidirectional fabrics consist of all fibers oriented in a single direction. Single direction run with no weave ensures that there are no gap is present between the UD fibers. Fibers mechanically best perform when the forces applied are along the direction of the fiber grains. Compared to woven fabrics, Unidirectional fabrics have higher fiber density in the selected direction which results in better mechanical properties [17].

Woven fabrics are made up of weaved fibers on a warp and a weft. Many different weaves are used with different visual and mechanical properties. Generally, woven fabrics are much easier to work with when compared to UD fabrics. During draping, woven fabrics tend to have better structural integrity due to interlaced fibers holding the fabric together. The most common and main types are plain weave, twill weave, harness satin weave, and spread woven tow. Depending on the application a certain type of weave might be more efficient to use. High-end automotive sector tends to use twill fabrics more than unidirectional counterparts because of the esthetic properties and the better workability during the draping process [18].

Due to the nature of the fibers, fiber-reinforced plastics are anisotropic materials. Anisotropic materials show different mechanical properties in each direction as shown in Figure 10. In reinforced polymer composites the direction of the fiber grain is usually oriented with the line of force to achieve the best mechanical resistance against the loads.

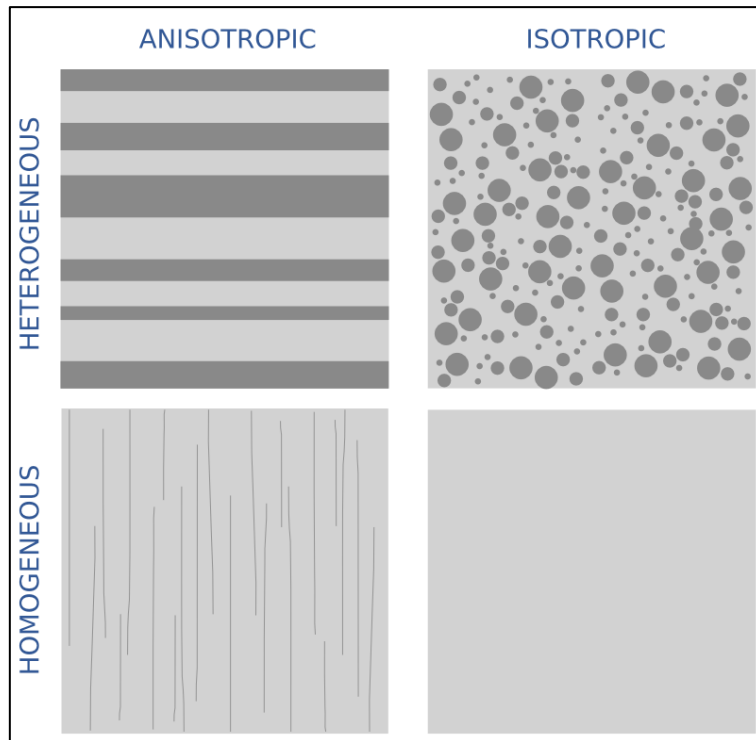


Figure 10. Heterogenous isotropy/anisotropy, Homogenous isotropy/anisotropy [70].

2.7 Honeycomb Sandwich Structures

Sandwich composite constructions are mainly used in aerospace and space applications due to low-weight requirements while maintaining a high in-plane stiffness, with a low cost of manufacturing. Composite sandwich panels consist of 3 main parts: The face sheet, core material, and adhesive film as given in Figure 11.

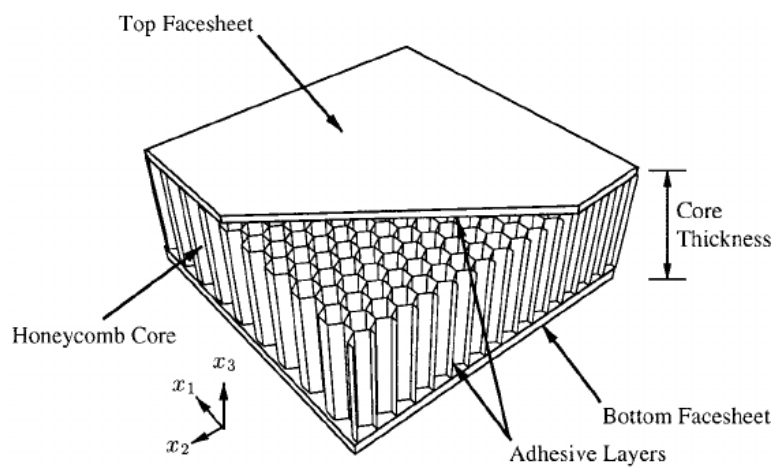


Figure 11. Schematic of a honeycomb sandwich panel with its main components [71].

The two thin, high-strength face sheets sandwich the thick core material in the middle. A layer of the adhesive film is used between the face sheet and core structure to ensure that the bonding interface is strong and can withstand against the shear loadings. Ultimately a sandwich structure acts as an I-beam as shown in Figure 12. The core material is the lightweight web that supports the load-carrying surfaces, the flanges. Due to the range of materials available, lightweight materials are the usual choice for the core. Being lightweight allows for the thicker core structures to be present in the sandwich without sacrificing the overall weight. As a result, an increase in the thickness of the core material increases the overall flexural stiffness of the structure. The use of a core material combined with high-strength surface sheets allows lightweight and stiff structures to be built efficiently [19].

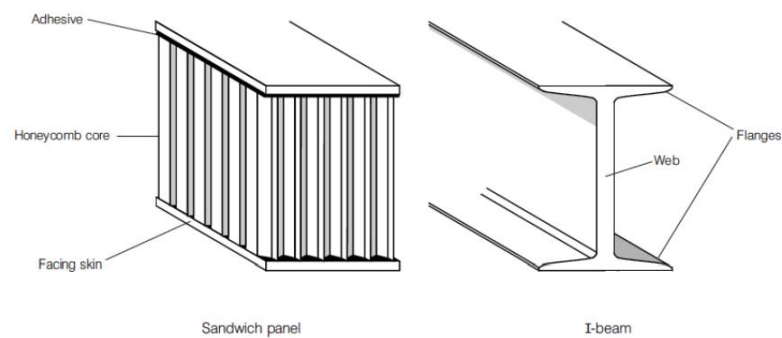


Figure 12. Side to side schematics of a sandwich panel and an I-beam. [72].

There is a wide range of materials available at the market for the selection of core structures. They can be categorized under aluminum honeycombs, Nomex honeycombs, thermoplastic honeycombs, and stainless-steel honeycombs.

A few examples commonly used materials are steel, aluminum, fiberglass, balsa, pvc, aramid and open and close cell foams. Based on the application, operating temperatures, electrical conductivity, magnetic properties, vibrational damping, humidity and loads, appropriate material selection can be achieved. This wide range of material

selection enables the engineers to tailor their needs with the appropriate materials to suit the design specifications [20].

When in-plane and bending loads are applied to the structure, the upper skin of the panel bends towards the direction of the force applied as shown in Figure 13. Due to the geometric properties, this bending results in the lower face sheets going under compression while the upper face sheet goes under tension. While the core structure does not carry most of the loads, it transfers the load through the thickness, carrying through-the-thickness shear loads. Stiffness and strength values of sandwich panels in terms of thickness are shown in Figure 14.

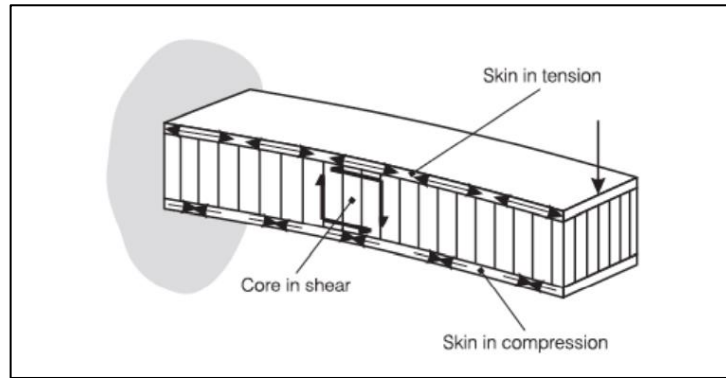


Figure 13. Sandwich panel under load. (The load is carried by the face sheets and the core structure is in shearing.) [73].

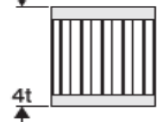
	Solid Material	Core Thickness t	Core Thickness $3t$
			
Stiffness	1.0	7.0	37.0
Flexural Strength	1.0	3.5	9.2
Weight	1.0	1.03	1.06

Figure 14. Sandwich panel stiffness, flexural strength, and weight for various core thicknesses [74].

Compared to balsa, open-cell foam and close cell foams, honeycomb structures offer greater stiffness through their thickness. This through-thickness stiffness provides increased support to the faces, therefore increases the overall flexural strength and rigidity. Other than the material itself the type of the cell structure plays an important role in the selection process too. The most common cell shape in the commercially available honeycomb is the hexagon. Hexagon is the most efficient shape to distribute the load evenly throughout the structure. The alternative cell types can be used for different applications. Different shaped core structures such as flex-core can have better drape ability than the standard hexagon cell core [21]. Various core types are given in Figure 15.

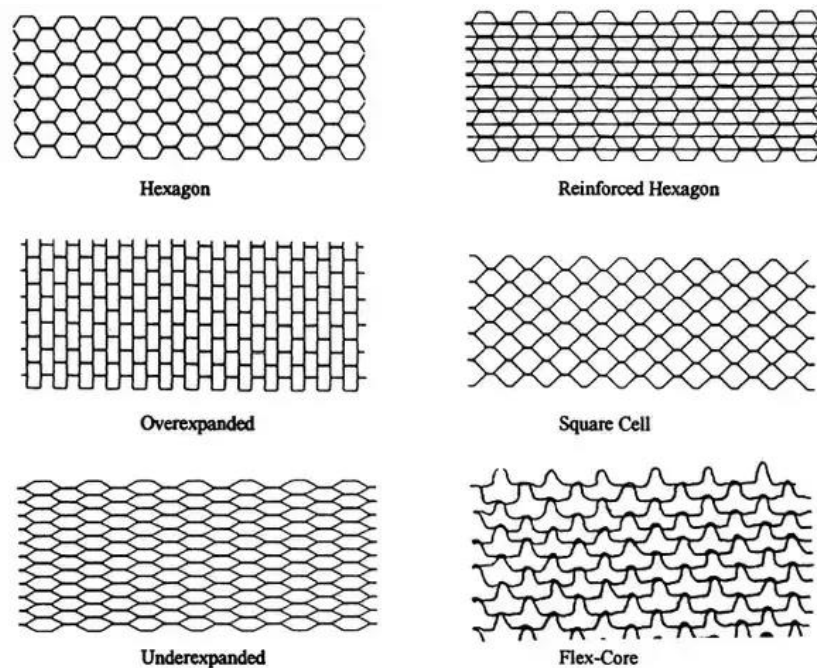


Figure 15. Various core structure cell types [22].

Honeycombs are stronger and more rigid in their length direction. The reason is that adhesive lines are aligned in the direction of the cell height and this direction strength and flexural stiffness are solely depend on the strength of the bond interface. Therefore, the direction of cell height is much weaker than the direction of the length. However, the

direction of cell thickness has the greatest compressive and tensile strength. These different behaviors and properties in each direction make honeycomb structures anisotropic [23].

2.8 Scanning Electron Microscopy (SEM)

As a result of various mechanical tests, scanning electron microscopy, one of the methods of analyzing composite topographic samples, enables the determination of the shape and size distribution of the parts that make up the object, and the determination of the number of elements and compounds. The scanning electron microscope method is widely used in the observation of damage mechanisms, especially in composite samples, since it can reach higher levels than the focal depth of the light metal microscope. With the SEM imaging method, images with the high surface resolution of nanomaterials in the nano-size range can be obtained [58]. In SEM microscope, scanning coils are used to scan the sample surface with the electron beam and obtain images. The signals generated by the electrons coming to the surface of the sample through the optical column and interacting with the sample are detected with appropriate detectors and provide various information about the sample, such as topography and composition. The SEM equipment which is used in this research is shown in Figure 16. However, this information is only taken from the point where the electron beam hits the sample. Scanning should be performed by moving the electron beam from one point to another in order to be able to examine and create an image at other points of the sample. Scanning can be defined as moving the beam at various positions on the sample surface by changing the current in the scanning coils over time. The response created by the beam moving in X and Y coordinates on the sample surface is monitored with the help of detectors. The image is created synchronously with the scan on the CRT with the system controlled by the same scan generator. In order to create an image, the area scanned in the x-y direction on the sample must also be created on the CRT screen at the same time. Every point on the sample is reflected on the CRT screen exactly. In the SEM microscope, in order to create the image, different types of signals separated from the surface as a result of electron and sample interaction must be collected and processed by the electronic equipment connected to the system. Detectors collect these signals and convert them into electrical signals. The signal generated in each half is transmitted to separate electronic circuits.

When the difference between these two signals is taken, an image reflecting the topographic characteristics of the sample is obtained, and when these two signals are collected, an image is obtained according to the chemical composition of the sample. While the image is obtained as a result of electron beam-sample interaction, the signal intensity perceived by the detector is used to adjust the brightness on the CRT screen. Black, low signal intensity; gray, medium signal intensity; white indicates high signal intensity.

Damage occurs when the principal stress affecting the core material in the sandwich panels exceeds the yield stress and this is called core failure. The types of failures seen in composite parts such as separation of the adhesive film between the core and face sheet layers, matrix and fiber breakage can be examined in detail with SEM. (59)



Figure 16. Leo SUPRA 35VP FEG-SEM measurement device [75].

2.9 Planar Green's Function Approach

In the selection of the radome wall material, the reflection loss and transmission loss values of the electromagnetic waves at certain frequency and incident angles are one of the determining performance criteria independently of the geometric structure of the radome [24]. After characterizing the transmission loss values, the optimum radome wall material can be designed in accordance with the geometry required by the application. There is more than one method where reflection loss and transmission loss values can be calculated by computational electromagnetic analysis of radome arrays with single and multiple dielectric wall structures. Planar Green's function method is the method that can give the most accurate approach and is the most computationally effective method [25]. Thanks to this method, the transmission loss values of a radome wall with C-type sandwich structure can be realized in different incident angles and a wide frequency band as shown in Figure 17.

In the Planar Green's function method, radome wall structures with multi-layered finite thickness arrays are implemented into the model as infinite 2-dimensional planes as shown in Figure 18, and the electromagnetic properties of dielectric layers can be defined separately. Thanks to the dielectric layer modeling with planar infinite dimensions, the performance of electromagnetic waves scattering through the radome wall can be simulated with good convergence. [26]

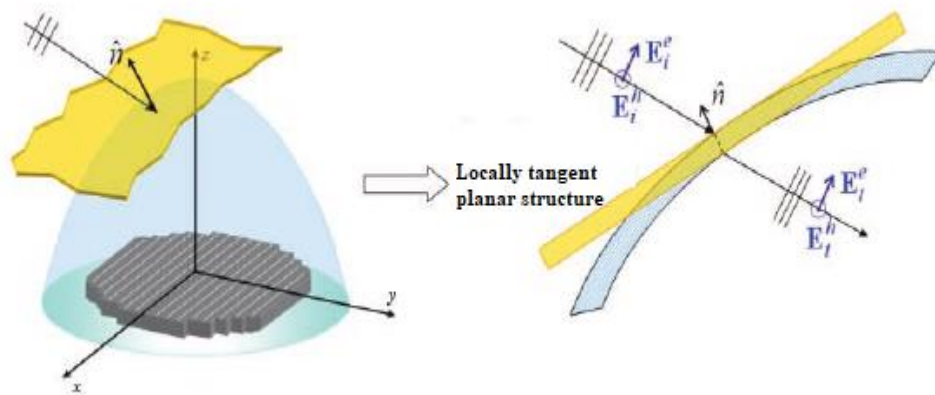


Figure 17. Radiofrequency wave acting on a spherical shape radome with specified incident angles and assumption of locally tangent planar structure [26].

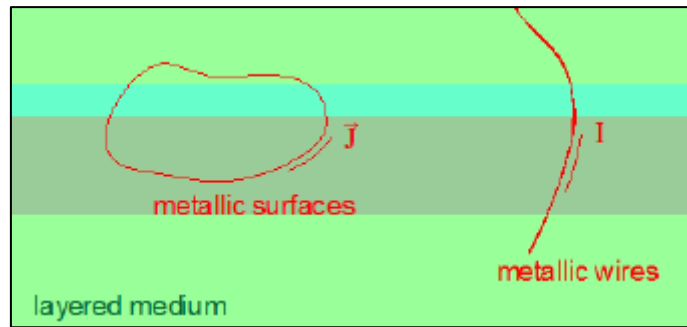


Figure 18. Radome panel multilayered medium in terms of Planar Green's theorem [26].

2.10 Quasi-static Indentation Tests

Radome wall structures in aircraft have performance requirements that are structurally required in addition to the purpose of electromagnetic waves reaching the antennas with the least amount of transmission loss by seeing a dielectric window between the air and the antennas. Some damage mechanisms such as fiber breakage, fiber debonding, matrix cracking, delamination, core crushing may occur in the sandwich panel's face sheet, core or the adhesive layer between face sheet and core due to the impact loads that radomes may encounter under operating conditions should be examined in detail during the design phase. Barely visible impact damages occur on the sandwich panel due to loads such as bird strikes, hail strikes, runway debris strikes, and maintenance tool drops that cause impacts at low velocity. Some researchers have carried out academic studies on quasi-static indentation tests in order to examine and characterize the damage mechanisms on the sandwich panel. Sorous [66] carried out quasi-static indentation tests on sandwich panels and conducted damage behavior studies with force and indentation depth data. However, it has been found that the damage due to static indentation is visibly the same as the damage caused by the impact. Oplinger and Slepetz [65] conducted quasi-static indentation tests on sandwich panel samples with graphite/epoxy face sheet and Nomex honeycomb core and conducted studies on impact resistance. As a result of this study, they found that the damage mechanisms obtained as a result of the impact tests with a small amount of quasi-static indentation tests are similar. They observed that the

applied load had a linear trend up to the first indentation stage when the core crushing damage occurred locally.

The factor that causes this difference to occur is the inertial forces under the impact loading state. As a result of this study, one of the most important outputs of the literature is that quasi-static tests can be used as a faster method instead of low-velocity impact tests to investigate the types of damage mechanisms that occur on sandwich panel samples [63].

2.11 Acoustic Emission (AE)

It is one of the test methods used to detect cracks and similar damages that occur due to the distribution of stresses in the internal structure of the parts. Although the acoustic emission method shows similar features with ultrasonic imaging methods, there are some differences between them. In the ultrasonic test method, the waves emitted from a transmitter along the part and reach a receiver and the signal cycle is completed. In this case, if the propagating wave passes through a crack or damage, its speed and amplitude value decrease due to the absorbed energy. When the time and velocity values of the waves that have not encountered the damage and passed through the damage are compared, the length of the damage on the part is calculated. In the acoustic emission method, the method of propagating sound waves over the part is also used, but the sensors in this method are generally called piezoelectric sensors. Due to the stresses acting on the sample shown in Figure 19, some damage and cracks occur in the sample after a while depending on the loading condition. The sound wave propagates in the form of an impulse due to the energy discharge at the time the damage occurs. Acoustic emission sensors measure this sound wave amplitude and other acoustic parameters. If more than one acoustic sensor is used on the sample, the location of the damage can be locally determined by obtaining the difference between the times when the sound wave reaches the surface from the point where the damage occurred and continues to move on the surface. The acoustic emission method is more efficient when the loading conditions on the sample occur dynamically and the damage activities that occur under low-stress density loading conditions may not be fully detected [27]. Acoustic emission sensors are

usually piezoelectric and convert mechanical waves into electrical signals between 30 kHz and 1 MHz frequency by parameterizing. Low-frequency acoustic waves are more easily noticeable on specimens made of composite material because of high attenuation. While evaluating the structural integrity of the material, information about the initial damage and progress of the damages is obtained thanks to the acoustic emission method. Acoustic waves are formed as a result of instantaneous deformation energy discharge resulting from damage in the sample. Acoustic waves formed on the specimen surface according to different frequency values can be recorded by piezoelectric sensors. Thanks to the acoustic emission test setup, even waves with very low energy can be easily obtained in certain frequency ranges. Composite sandwich panel materials are generally exposed to out-of-plane loading conditions under operating conditions, and failures such as delamination occur in the interphase regions, which are relatively weaker parts [28]. It is important to determine this and similar failure criteria because of the effects of delamination on the stiffness of the sandwich panel [29]. Acoustic emission, which is one of the non-destructive methods among the in-situ damage assessment methods on sandwich panels, can be applied more easily than other methods. One of the most important features of acoustic emission is to recognize the damages on the sample in real-time and classify them according to the damage type [30-31]. The acoustic emission method is a natural method created by transient elastic waves that occur from instantaneous energy discharge in the material [32].

Various damage mechanisms such as fiber breakage, matrix breakage, delamination, and debonding occur as a result of the loading of composite materials under various loads [33-34]. One of the most important points in the acoustic emission method is to distinguish different signals created by different damage mechanisms. The researchers carried out some research on different parameters of an elastic wave such as counts, acoustic emission energy, and amplitude in order to distinguish signals and determine their damage mechanisms [35-36]. In the literature, studies of Kenji and Ono [37], one of the supervised clustering methods was used in the classification of damage mechanisms of carbon-reinforced polymer composite materials by the k-nearest method. Supervised recognition methods are used if the number of damage mechanisms occurring in the material is known in advance, while unsupervised recognition method is used if there is no previous knowledge about the damage mechanisms. The neural network

method has been used in some studies in the literature to classify damage mechanisms different from acoustic emission signals [38-39]. Although classification methods performed with neural networks give correct results, they are not very efficient in terms of computational time and they have performance limitations due to the number of neurons that need to be determined in advance and the network structure [40]. The applications given in the above literature examples are mostly carried out with acoustic emission signals in the time domain, but there is also important information for evaluating the damage mechanisms in the signals in the frequency domain. The wavelet transformation method, which is used by many researchers, has been used efficiently to examine the signals in the time-frequency domain with the acoustic emission method [41-42].

Although there are previous application using the acoustic emission method regarding the investigation of the damage mechanisms of composite materials in the literature, the number of studies conducted on sandwich panels is less. Until now, the studies of a small number of researchers have included the examination of the acoustic emission signals generated on sandwich panels. Quispitupa et al. [43] included the acoustic emission signals arising under fatigue loading conditions of sandwich panels in their research by using energy and amplitude parameters. According to the results, it is possible to classify damage mechanisms in sandwich panels by the acoustic emission waveforms.

The Keizer effect, which is named after the researcher who carries out acoustic emission studies on the materials with the electronic test setup, is one of the main features of this method. These types of acoustic emission waves cannot be reproduced when there is no load condition greater than the previously applied load. In the research called felicity effect, it has been shown that when a less or the same loading condition is achieved than the previous one, acoustic emission signals are generated and can be recorded during the experiment [44]. These types of acoustic emission waves emerge in the material and vibrations created by the stress reaching the surface are detected by transducer sensors. Considering the propagation patterns and waveform structures on the material, we can divide the acoustic emission waves into three types. The wave type that occurs as a result

of the overlapping of the resulting acoustic emission waves and where the values in the amplitude graph are seen in a fixed way is called the continuous acoustic emission wave. It is generally regarded as noise caused by the rubber on the sample or other environmental factors. Burst type acoustic emission waves arise as a result of damage criteria such as fiber breakage or delamination occurring in the sample under the loading condition. The noise waves, which have a smaller amplitude than the acoustic emission waves that occur during the damage, should be carefully detected and filtered when evaluating the results. PZT sensors as given in Figure 19, made of ceramic material are frequently used in a wide frequency band in acoustic emission applications.

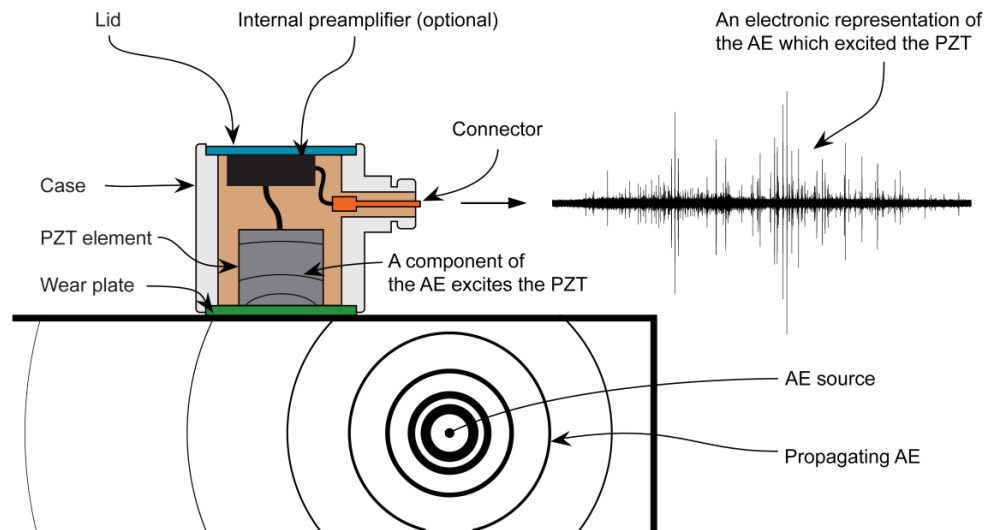


Figure 19. Schematic of acoustic emission testing and PZT transducer [76].

While measuring with the PZT sensor, the surface quality of the composite sample used and the way the sensors are adhered to the surface significantly affect the precision of the measurement [45]. Due to the working principle of ceramic transducers, the normal of the transient waves on the surface as a result of damage and the normal of the sensor surface must be parallel to each other. The same cannot be said for the reflected waves due to vibration, even if the stress components caused by the damage reach perpendicular to the surface normal of the sensor. While choosing the transducers used in the experiments, the frequency range of the waves that will occur on the part, and the operating frequency curves of the sensors should be compatible. Sensors can work as a

displacement transducer when there are waves propagating at low frequencies on the sample, but it acts as velocity sensors when the incoming acoustic waves at high frequencies [46]. The Hsu-Nielsen calibration method is used to check the connection and sensitivity of the transducer sample. The working principle of this calibration method is provided by the propagation of a broken pencil tip on the sample surface as if it were a mechanical acoustic wave. Hsu states that a pen tip with a diameter of 0.5 mm should be used during the use of this method and indicates that when the pen tip diameter is changed, the characteristic of the acoustic emission waves changes due to the change in the structure of the pen. Teflon should be placed between the pen and the sample surface to obtain reproducible results in terms of accuracy [47]. In the recent studies, the researchers examined various parameters of the signals in order to obtain meaningful results from acoustic emission sensors. Researchers made evaluations about the damage mechanisms by interpreting the acoustic emission data they obtained with different classification and statistical methods. We can evaluate acoustic emission waveform data in 3 main groups as frequency-based, hit-based, and activity-based.

Signals that occur in the form of sudden and time-dependent changes in acoustic emission signals are called activity-based. The parameters that are important in this type of acoustic emission signal are the number of hits obtained and the energy of the signal [48-49]. Usually, the obtained number of hits data are cumulatively calculated and analyzed. It is a method used for acoustic emission signals caused by friction in the sample [50].

When a waveform is formed that fully meets the predetermined parameters such as amplitude and time in the acoustic emission electrical test setup, it is evaluated as a hit and this type of waveform is called hit-based. Thanks to being evaluated as a waveform hit, it is separated from the noise waveforms originating from the test setup or other environmental factors. Since hit-based waveforms are stress waves, they are evaluated separately from other continuous waveforms recorded during the experiment. Various methods are used to evaluate a waveform as a hit, the most common of which is accepting waveforms with an amplitude value below or above a certain threshold decibel value. When this technique is evaluated in terms of time, it has three important parameters.

These parameters are called hit definition time (HDT), hit locked out time (HLT) and peak definition time (PDT). According to the specified parameters, only when a waveform reaches the required values in terms of time, the sensors save the waveform, and a hit is obtained. There are components such as amplitude, energy and rise time in the hit waveform, which has values above the threshold level [51]. The relationship between these properties is shown in Figure 20. The results are interpreted by using statistical processes such as adding or removing these components while processing the waveform data obtained in the tests where acoustic emission measurements are performed.

The waveform properties obtained from the process can then be turned into histogram graphics and comments can be made about the damages that occur. The values obtained in the histogram graph are an important evaluation tool in terms of the amplitude differences they have about the damage mechanism in the sample.

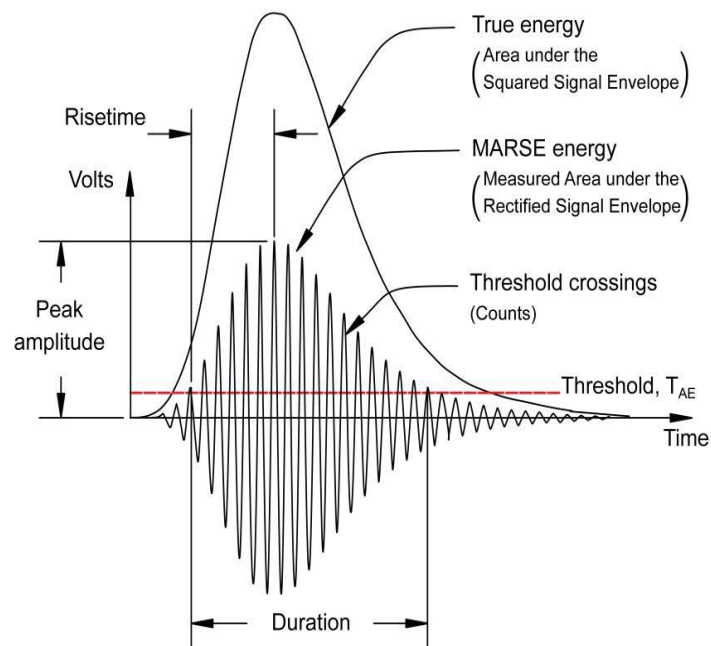


Figure 20. Acoustic emission hit based waveform features [77].

The waveform features obtained from the acoustic emission results can be plotted concerning each other, and correlations can be created between them, which allows the damage mechanism to be determined. In this way, instead of examining all the data points obtained by the sensors, an examination can be made only among the hits caused by the

damage mechanism. Since the elastic waves formed on the surfaces of the composite materials provide high amounts of attenuation, the waves closer to the sensor can be distinguished from the distant ones. While performing frequency-based waveform analysis, computationally data storage is excessive. frequency-based waveforms include many mechanical parameters related to the material. During the extraction process of the waveforms, the modulus values of the material can also be calculated by obtaining lamb waves as an example. There are two types of lamb waves, S_0 and A_0 . S_0 mode is called the lowest order symmetric flexural, and A_0 mode is called asymmetric extension mode. Different analysis techniques of these lamb wave types with different properties are called modal acoustic emission [52-53]. There are many studies in which the acoustic emission measurement method was used during the tests of composite materials [54-55]. Those found in the range of 100-350 kHz according to the frequency of waveform hits are associated with the matrix cracking damage mechanism. Fiber breakage damage was observed in the acoustic emission data in the frequency range of 350-700 kHz [56].

CHAPTER 3

3. Electromagnetic Transmission Performance of Radome Sandwich Panels

In this part of the thesis, the frequency-dependent electromagnetic transmission and reflection loss performances of the radome sandwich specimens consisting of aramid, E-glass skin and Nomex honeycomb core are evaluated both experimentally and numerically. Specimens are subjected to free space electromagnetic tests in the frequency band of C, X, Ku and K, besides their relative permittivity and dielectric loss values are obtained. Electromagnetic performances of specimens and their constituents (face sheet and honeycomb) are compared while verifying EMC (Electromagnetic Compatibility) simulation results with the experimental outcomes. Research steps are shown in Figure 21.

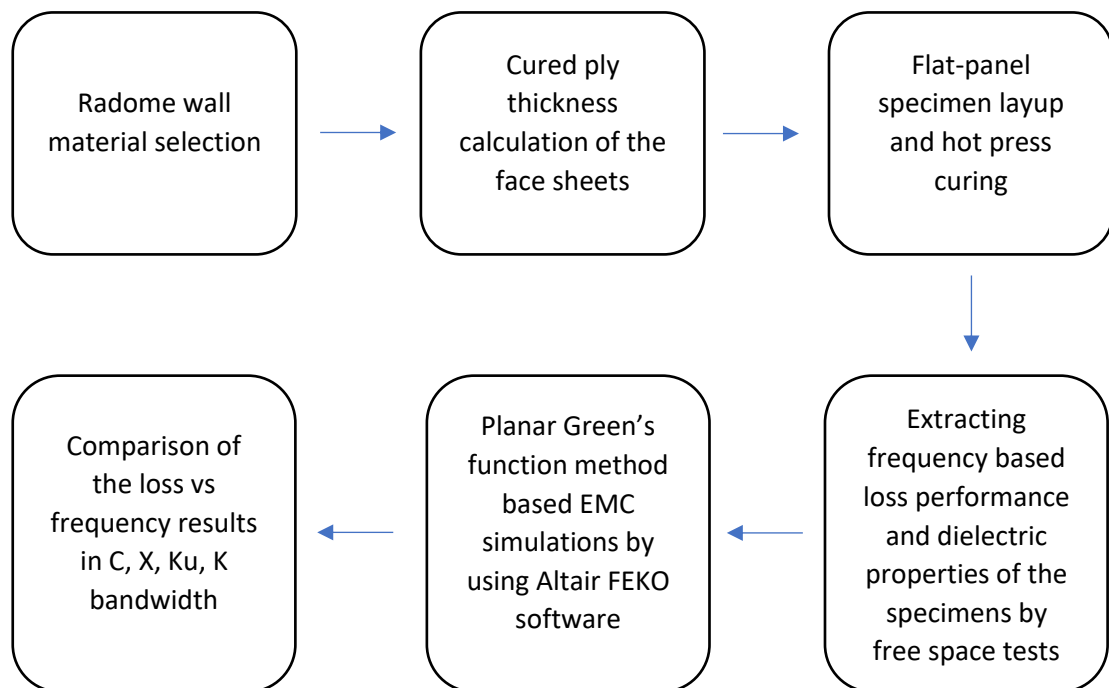


Figure 21. Electromagnetic performance assessment of the research steps.

3.1 Experimental Study

E-glass and aramid fabric composite materials are selected to be able to represent the radome material widely used in today's aerospace applications. To this end, two different sandwich panels have been produced. Prepregs with EF12 epoxy-based resin system and properties listed in Table 3 are purchased from Kordsa company and used as face sheet material in sandwich panel manufacturing. Nomex[®] honeycomb is used as core material.

Table 3. Detailed information and properties of radome sandwich panel face sheet plies.

Design	Prepreg Code	FAW (gsm)	Fiber Type	Weave Type	Warp End Count (Ends/cm)	Warp End Count (Ends/cm)	Warp & Weft Yarn (dtex)	Tg (°C)	Resin Content (%)
1	KEF12 AR 3140 PL400	400	Aramid	Plain	6.4	6.4	3140	>180	35%
2	KEF12 E-Glass PL380	380	E-Glass	Plain	6.4	6.3	3000	>180	35%

To be able to conduct electromagnetic wave transmission tests on the sandwich panel samples reliably, it is important to use a sandwich panel with identical thickness. For calculating the cured ply thickness of the face sheets of the samples, the rule of mixture formulation is used by calculating the resin content weight ratio of prepregs, fabric areal weight (W) and fiber density (ρ_f) and matrix density (ρ_m) as given in Equations 14 and 15 where n denotes the number of plies, W_f is the fiber areal weight, V_f and V_m are the volume fractions of the fiber and matrix, respectively.

$$\text{Cured Ply Thickness} = \left(\frac{n \times W}{1000 \times \rho_f \times \rho_m} \right) \times \left[\frac{\rho_f}{W_f} - (\rho_f - \rho_m) \right] \quad (14)$$

$$W_f = \frac{\rho_f \times V_f}{\rho_f \times V_f + \rho_m \times V_m} \quad (15)$$

As such, the skin thicknesses of the radome sandwich panel samples are obtained as a result of cured ply thickness calculations. The typical geometrical dimensions of the sandwich radome structures used in today's industry include 0.762 mm skin and 5.8 mm honeycomb core thicknesses [2]. In this study, the cured ply thickness of the face sheet is calculated to be 0.75 mm for both aramid and E-glass prepreg materials and accordingly, the number of plies for both face sheet types are determined. The honeycomb core

material is selected to be 5.5 mm thick. Both aramid and E-glass prepreg materials are chosen to have %35 weight resin content.

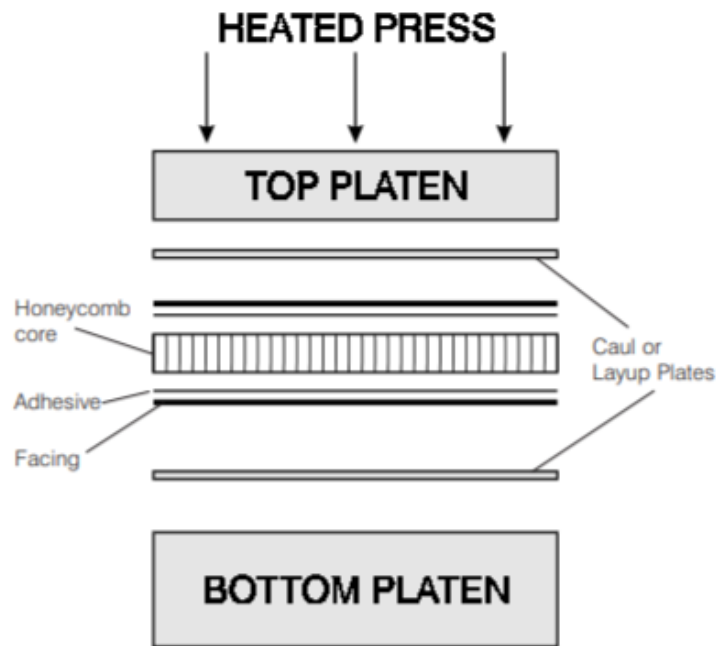


Figure 22. Schematic representation of the hot press curing process and layer layout [78].

The hot press curing method, which is illustrated schematically in Figure 22, is chosen as the production process in order to achieve the desired thickness values of the samples and to reduce the void content amount that may occur during the production. The hot-press consists of two heating platens located at the top and bottom and 2.6 bar pressure is continuously applied during the curing process of the sandwich panel. The resin system of the prepregs is chosen to be suitable for the hot press curing process, where temperature ramp vs. appropriate pressure profile has been provided by the manufacturer [82]. An epoxy-based structural adhesive film 3M AF163-2 is used to ensure that the face sheet and core layers adhere to each other and act as a solid sandwich panel. The adhesive film is cured in accordance with the curing process of the face sheets.



Figure 23. Waterjet cutting free space test specimen preparation.

The large panel produced by hot-press with the dimensions of 3m by 1.3m was cut into several specimens for structural and electromagnetic test samples with the help of a robotic water jet without inducing any possible cutting damage as given in Figure 23.

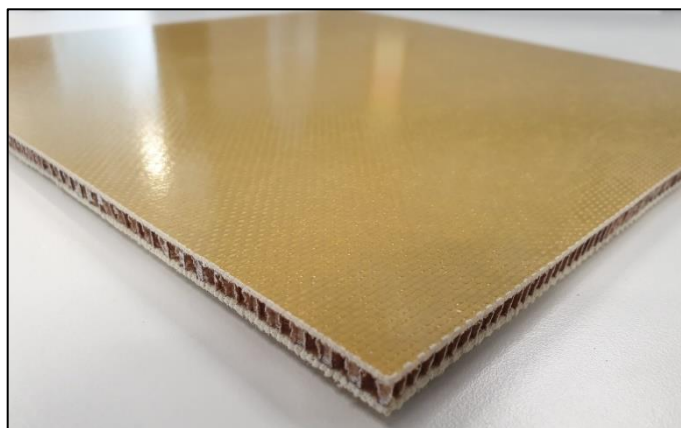


Figure 24. Aramid skin and honeycomb core radome sandwich panel free space test specimen.

Laminated samples are also manufactured using both face sheet types as shown in Figures 25 and 26. The specimens extracted from these laminates are cut into to the sample dimensions for measuring the dielectric coefficient and loss tangent values of the constituents through using free space test method. The obtained results are employed as an input parameters for the EMC simulation model.

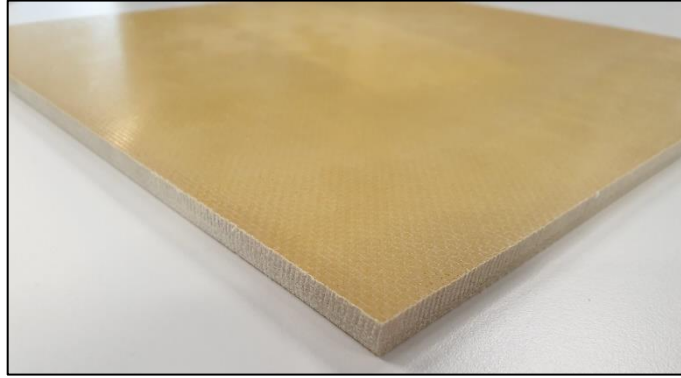


Figure 25. Aramid laminate free space test specimen.

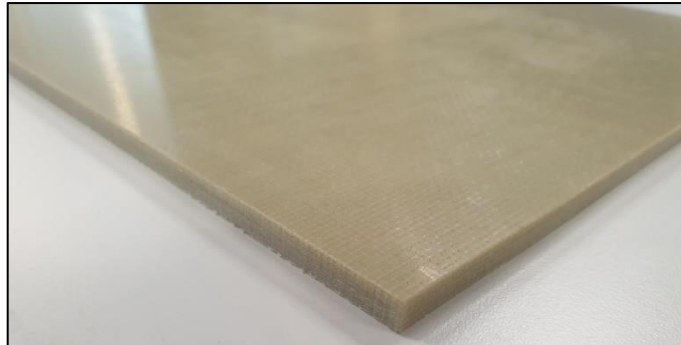


Figure 26. E-glass laminate free space test specimen.

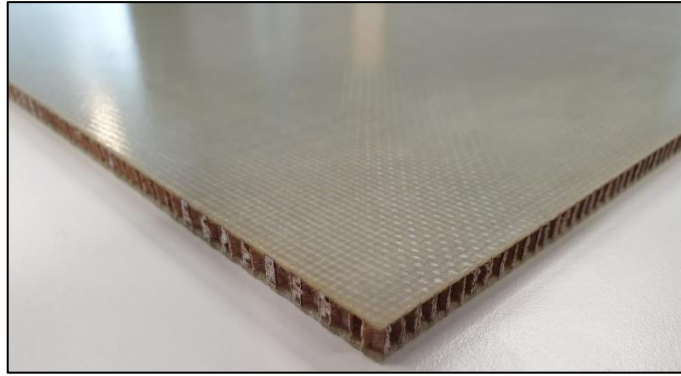


Figure 27. E-glass skin and honeycomb core radome sandwich panel free space test specimen.

The hot press forming method is one of the most preferred approach in composite part manufacturing with the flat-panel geometry due to its effectiveness in reducing the void content in the final part. As briefly mentioned above, in this method, the core, prepreg, and adhesive layers are laid between the upper and lower mold as illustrated in Figure 28.



(a)



(b)

Figure 28. Aramid and E-glass honeycomb panel hot press layup.

3.2 Experimental Setup

The free space method test setup is used to measure the electromagnetic wave transmission and reflection performances of the sandwich panels and their constituents individually in the frequency range of C, X, Ku, and K bands (5.85-25 GHz). The samples that are prepared for the test have a flat geometry with a dimension of 30 cm x 30 cm as shown in Figures 24-27. During the tests, dielectric coefficients and loss tangent values of the constituents are also measured in the frequency range of 8-25 GHz.

The permeability (loss tangent) and permittivity (dielectric constant) values are obtained through utilizing the transmission and reflection waves, which occurs as the electromagnetic waves travel along the thickness of constituent materials, namely, face sheets and the core. The free space test setup used in this study is shown in Figure 29 and essentially contains two horn antennas such that one of which is a transmitter and the other is a receiver that enables electromagnetic wave transmission at specified frequencies.

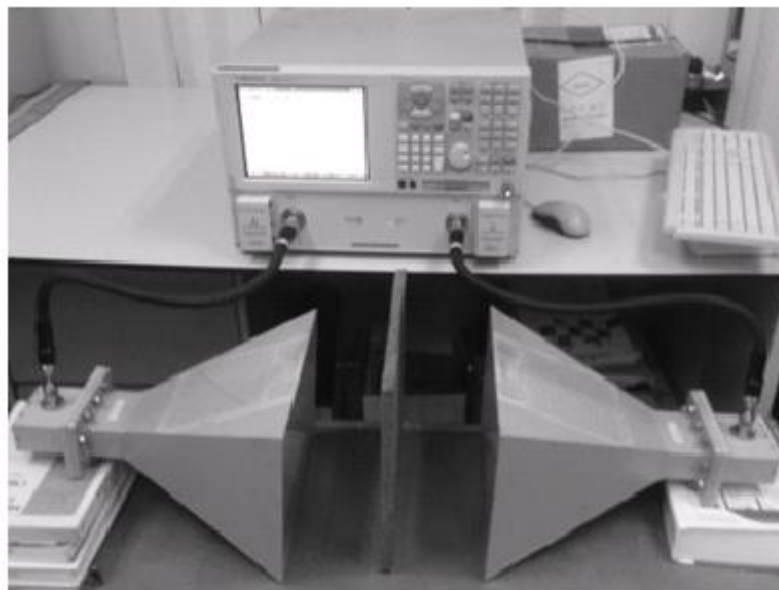


Figure 29. Free space test setup [79].

In addition to the antennas, one of the most important components of the test setup is the network analyzer. Network analyzers can measure by giving instant reaction to electromagnetic waves in the frequency range of 300 kHz to 110 GHz [10]. The network

analyzer consists of three basic components, i.e., processor, detector, and the source that generates the signal itself as given in Figure 30.

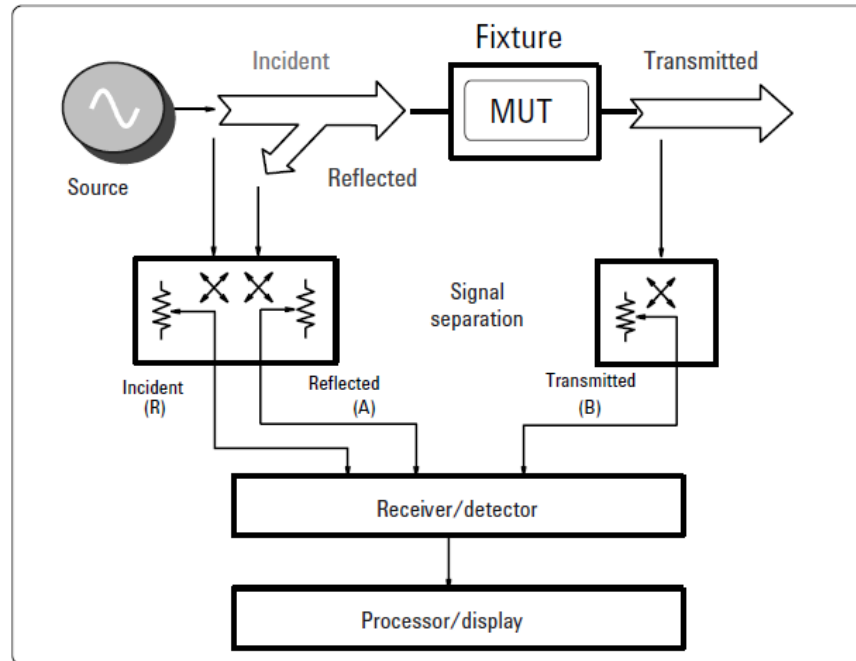


Figure 30. Component diagram of the vector network analyzer [10].

During the test, a wave at a certain frequency is generated by the signal source and directed towards the sample material. Electromagnetic waves that are transmitted through and reflected from the sample material are detected by the receiver. The reflected and transmitted waves are compared to the source signal in terms of their frequencies within the network analyzer. In this way, the magnitude and phase values of the wave at the detected frequency are obtained. By repeating this step for each frequency increase or decrease, the transmission and reflection values are calculated in terms of a frequency-dependent function according to the waves in the frequency range measured.

3.3 Electromagnetic Simulation

The experimentally measured electrical material properties are used as input parameters for numerically modeling electromagnetic compatibility for which Hyperworks Feko[®] software is utilized as a solver. During the simulations, while defining the plane wave affecting the sandwich panel sample of the radome structure, the

mathematical variables are defined according to Planar Green's function theorem as shown in Table 4.

Table 4. Input parameters for the electromagnetic transmission simulation.

Variable Name	Value	Unit	Expression
Permittivity of free space	8.85×10^{-12}	F/m	-
Speed of light in free space	299792458	m/sec	$\frac{1}{\sqrt{\epsilon_0 \times \mu_0}}$
Permeability of free space	1.26×10^{-6}	H/m	$\pi \times 4 \times 10^{-7}$
Ratio of a circle's circumference to its diameter	3.141592654	-	-
Characteristic impedance of free space	376.7303135	Ohm	$\sqrt{\frac{\mu_0}{\epsilon_0}}$

For numerical EMC modeling of the sandwich panels, each domain, namely, free space, face sheet, and honeycomb core layers are defined as distinct dielectric medium as shown in Figure 31. Plane-wave frequency values acting on the sandwich panel are defined as the boundary condition in the range of 5.85-25 GHz with 1836 numbers of discrete data points. The plane-wave has a linear polarization angle and travels along the z-direction as show in Figure 31 with the magnitude of 1,500,000 V / m. In modeling sandwich panel layers, the multilayer substrate option of the HyperWorks Feko software is used. The parameters utilized in the software for the individual layers are presented in Figure 32 and Figure 33 for E-glass and aramid sandwich panels, respectively.

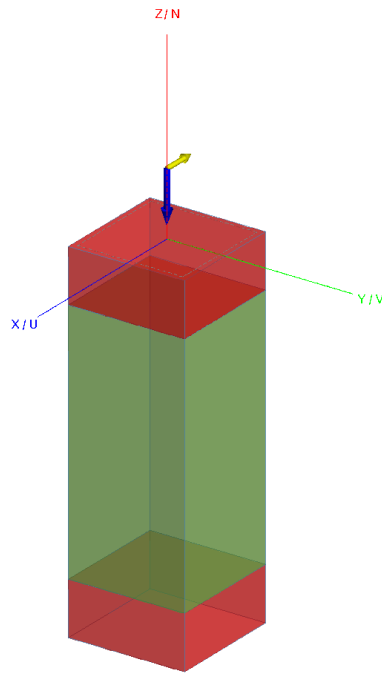


Figure 31. Numerical model for electromagnetic transmission simulation of radome sandwich panel.

	Media preview	Ground plane	Thickness	Medium
Layer 0		None	+inf	Free space
Layer 1		None	0.75	eglass
Layer 2		None	5.5	nomex
Layer 3		None	0.75	eglass
Layer 4		None	-inf	Free space

Figure 32. Multilayered substrate parameters of the E-glass radome sandwich panel model for the electromagnetic transmission simulation.

	Media preview	Ground plane	Thickness	Medium
Layer 0		None	+inf	Free space
Layer 1		None	0.75	aramid
Layer 2		None	5.5	nomex
Layer 3		None	0.75	aramid
Layer 4		None	-inf	Free space

Figure 33. Multilayer substrate parameters of the Aramid radome sandwich panel model for the electromagnetic transmission simulation.

3.4 Results and Discussions

In this study, recall that the dielectric coefficient and loss tangent values of the samples in the frequency range of 5.85-25 GHz are measured by utilizing the free space tests method. The electrical material properties of individual layers of the radome sandwich panels are obtained and are used as material inputs during the numerical analyses to simulate transmission and reflection loss.

The dielectric constant of the E-glass on a ply basis follows a linear horizontal curve between 5.85-25 GHz and has a value of approximately 4.75 as shown in Figure 34. Aramid prepregs, on the ply basis, draw an almost constant curve in the same way and has a value of approximately 3.5. Nomex honeycomb core with its hollow structure, on the other hand, is the most insulating and ideal material among the samples with a dielectric coefficient of approximately 1.0. According to the dielectric coefficient graph that is shown in Figure 34, considering only the ply basis, the more ideal material for radome design is found to be aramid than E-glass, while honeycomb as a core material has a very low dielectric coefficient value.

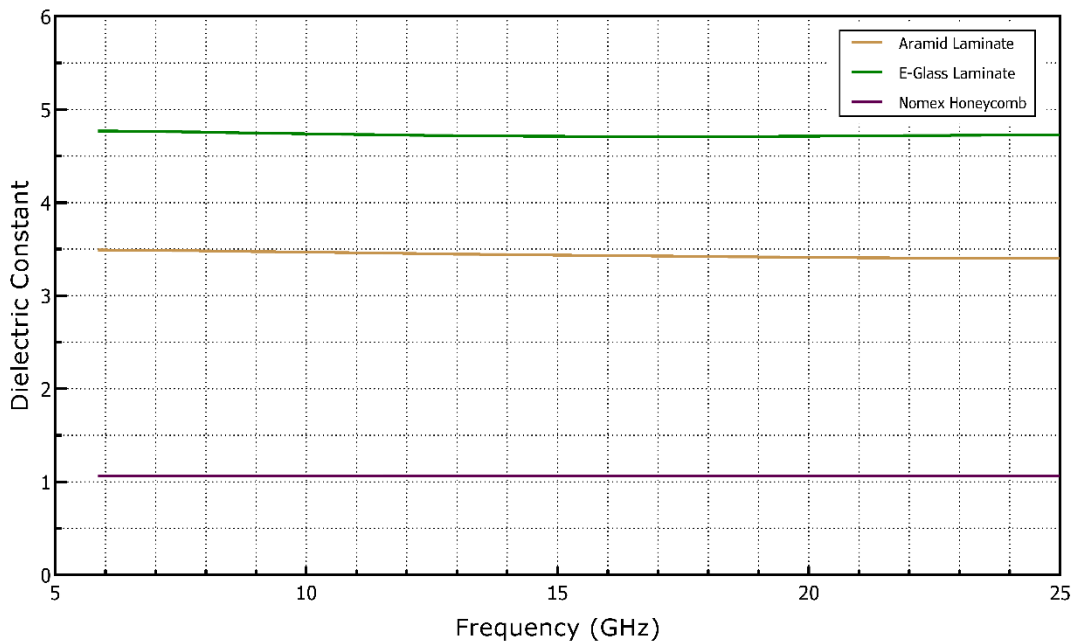


Figure 34. Dielectric constant results of the free space test.

The second finding from the free space tests that aramid prepreg ply has a loss tangent value of about 0.026 while E-glass prepreg ply has a loss tangent value of about

0.017 as given in Figure 35. Since the low loss tangent value is the desired electrical property in the choice of radome material, E-glass face sheet material is considered more ideal than aramid. Lastly, the honeycomb core material has a loss tangent value of approximately 0.002. As previously stated in the dielectric coefficient comparison, there is a huge difference in the loss tangent between the face sheet materials and the honeycomb core due to its hollow structure.

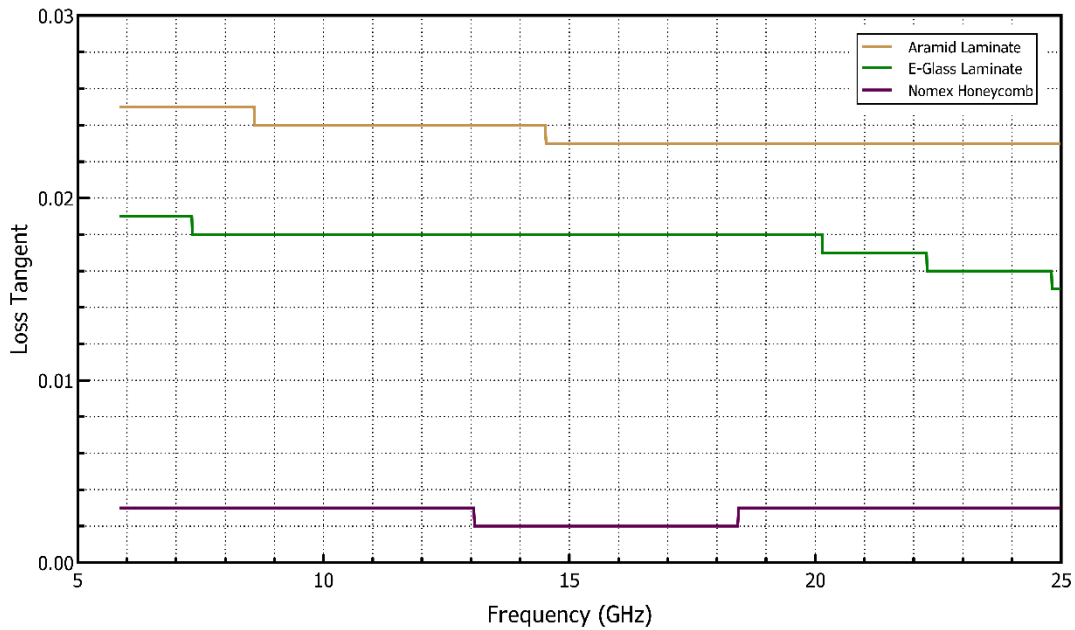


Figure 35. Loss tangent results of the free space test.

In Figure 36, the frequency-dependent transmission loss values that are obtained by free space test measurements and EMC simulations of E-glass and aramid sandwich panel samples were plotted comparatively. It is seen that the transmission loss curve of the samples fluctuates according to the frequency bands. In order to better characterization of the electrical transmission performance of the samples, examinations are carried out according to each frequency band. In the frequency range that is associated with the C band [5.85-8 GHz], the transmission loss ratios of the aramid and E-glass panels have an average value of 0.24 dB and 0.53 dB, respectively. As a result, the aramid panel sample possesses a better electrical transmission performance in the C frequency band. In the continuation of the test the frequency intervals of 8-12 GHz which implies the X band is discussed. The transmission loss of the aramid panel is calculated at an average value of 0.20 dB, while the E-glass panel transmission loss is calculated as 0.22

dB. It is also depicted by the experimental and simulation results that both of the sandwich panels have a quite insignificant transmission loss difference within the X frequency band. In the frequency range of the Ku band (12-18 GHz), the transmission loss curve of the aramid and E-glass panels have a parabolic downward trend. One can easily see that the transmission performance gap between the samples increases in the Ku frequency band to the advantage of the aramid panel. According to results obtained in the frequency band of K (18-25 GHz), both samples have the lowest electrical transmission performance values obtained throughout the tests that are 3.6 dB and 6.2 dB respectively for the aramid and E-glass. Eventually, it has been concluded that the optimum operating frequency range of both radome sandwich samples is the X frequency band where transmission loss values are the least. The second major finding is that the excellent agreement of the experimental and EMC simulation frequency-based transmission loss results.

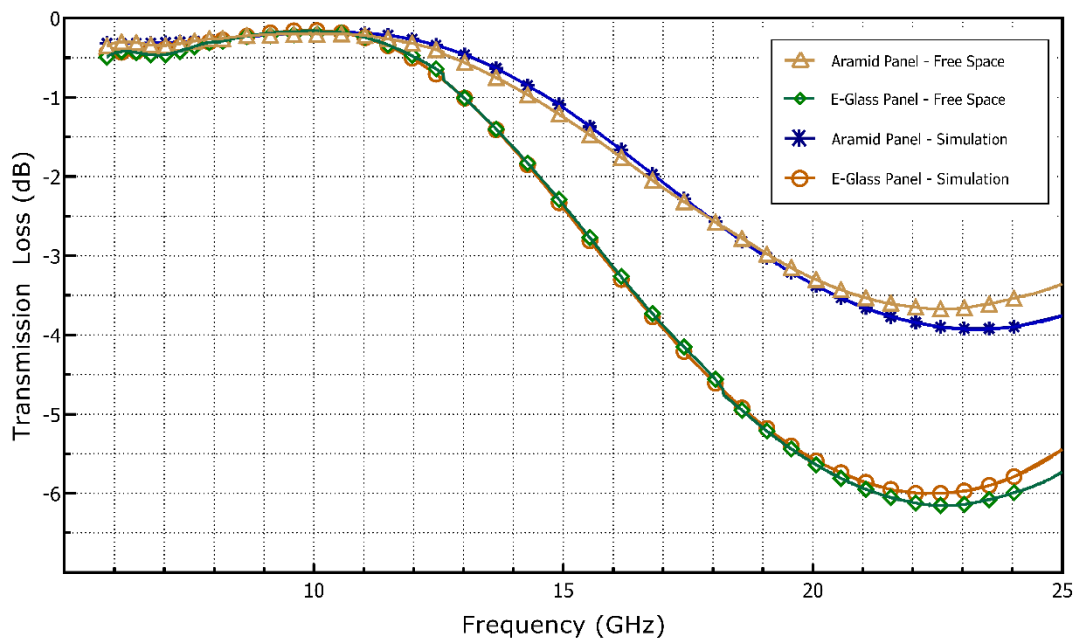


Figure 36. Comparison of free space test and electromagnetic simulation results for the transmission loss.

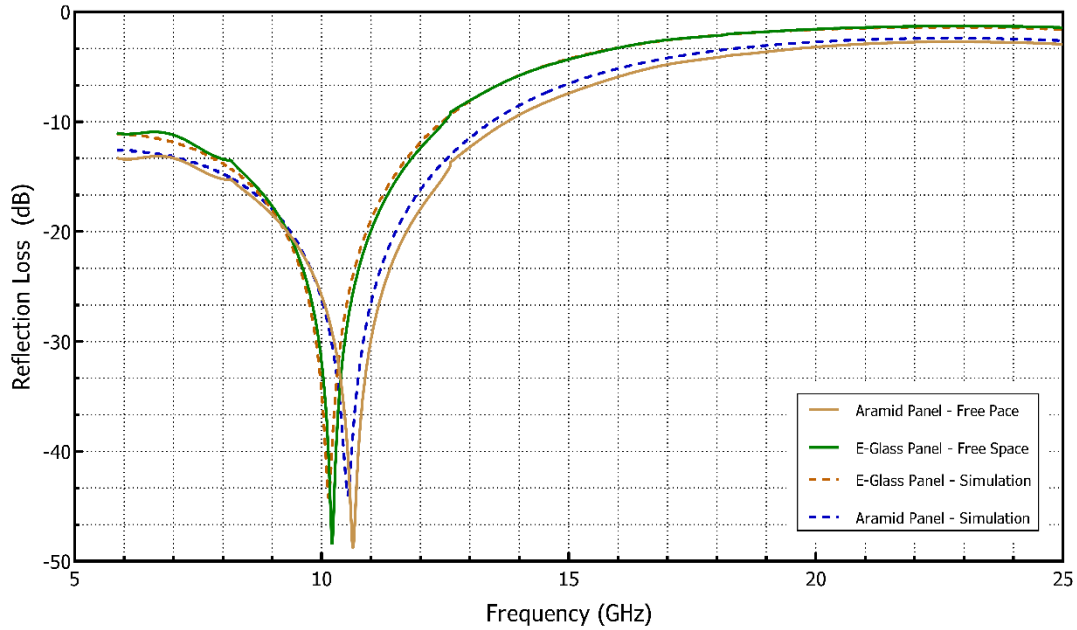


Figure 37. Comparison of free space test and electromagnetic simulation reflection loss results of the specimens.

Another way to compare the electromagnetic performances of radome materials is the interpretation of the reflection loss values. As shown in Figure 37, the free space test and EMC simulation reflection loss results of the samples are plotted in the frequency domain. At the beginning of the test, the E-glass sample has a relatively weaker electromagnetic performance against the aramid panel with a reflection value of approximately -11 dB. In the continuation, both samples get low reflection loss values and reach their optimum electromagnetic performance at 10-12 GHz frequency range. In coincidence with the lowest reflection loss values, both samples have the lowest transmission loss values in the same frequency range as previously mentioned. Towards the end of the free space test are approached, the reflection loss values of both samples increase and this is evidence that they do not show the desired radome electromagnetic performance values in the frequency range of 13-25 GHz. As a result, the experimental reflection loss values and the values obtained as a result of the EMC simulations coincide perfectly.

CHAPTER 4

4. Damage Characterization of Radome Sandwich Panels

This research is about the failure characterization of barely visible damages caused by low-speed impacts in radome sandwich panel structures with the quasi-static indentation tests approach. During the tests, several types of composite failure were observed in the face sheet, core, and interphase layers. Thanks to the piezoelectric transducers attached to the upper surface of flat sandwich panel samples, various acoustic emission parameters were analyzed according to the severity and type of damage. The damage clustering results obtained were verified by scanning electron microscopy images of the damaged areas.

4.1 Materials and Manufacturing of Sandwich Panels

The sandwich panels subjected to quasi-static indentation tests are made of Nomex[®] honeycomb core and E-glass or Aramid face sheet and manufactured through the hot-press method whose production details are provided in the previous chapter. The mechanical and electromagnetic transmission free space tests are conducted on the same specimens cut from the sandwich panels through water jet cutting system to the dimensions of 100 x 150 mm as given in Figure 23.

4.2 Experimental Test Setup

Quasi-static indentation tests are performed using a universal tensile machine (Instron 8803 model) with a load cell capacity of 250 kN under the displacement control of 0.5 mm/min. The indentation compression force is applied on the samples utilizing a hemispherical indenter of 16 mm tip diameter. The specimens are simultaneously clamped on the table from its four corners to circumvent its movement due to the applied

compression force. At the bottom surface of the fixture is left a rectangular gap of 80 x 130 mm to allow for the deflection of the specimen vertically.

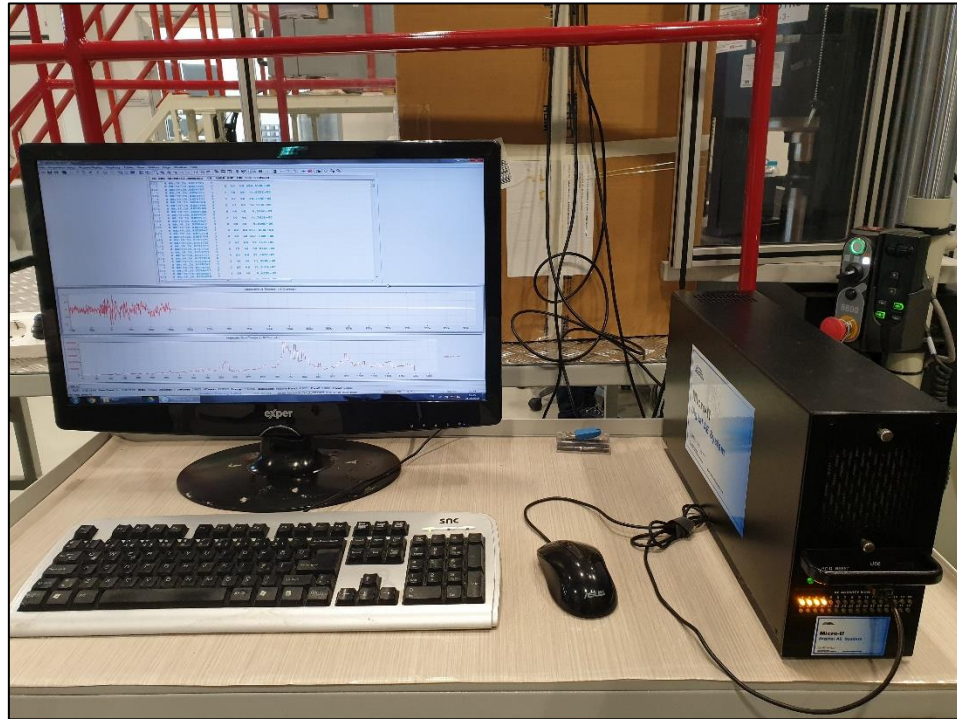


Figure 38. Mistras acoustic emission test setup.

As presented in Figure 39 (a), the piezo electric transducer acoustic emission sensors are mounted on the top surface of the specimen with a hot silicon thereby ensuring reliable acoustic coupling between the sensor and the indentation locations. Elastic waves generated due to the micro damages at various locations of the specimen during the test are acquired through employing Mistras PCI-2AE the acoustic emission setup with wideband sensors (PICO-200-750 kHz, Mistras) as shown in Figure 38. To amplify the output signal of the sensors, a pre-amplifier Mistras 0/2/4 with the gain of 20 dB is used. The acoustic emission waveforms occurring on the sample are limited to a 45 dB threshold and the waveforms have 50 microsecond peak definition time (PDT), 100 microseconds hit definition time (HDT), and 200 microseconds hit lockout time (HLT) as acoustic emission data acquisition parameters. A sampling rate of 40 MSPS is used for each of the acoustic emission sensors and the noise in the waveforms is removed by

applying *Bessel* band-pass filtering. To calibrate the acoustic emission sensors, the pencil lead break method is applied according to the ASTM E976-10 standard before each test. To prevent any possible source of noise from the clamp regions, a rubber material between the specimen surface and the fixing clamp is used.

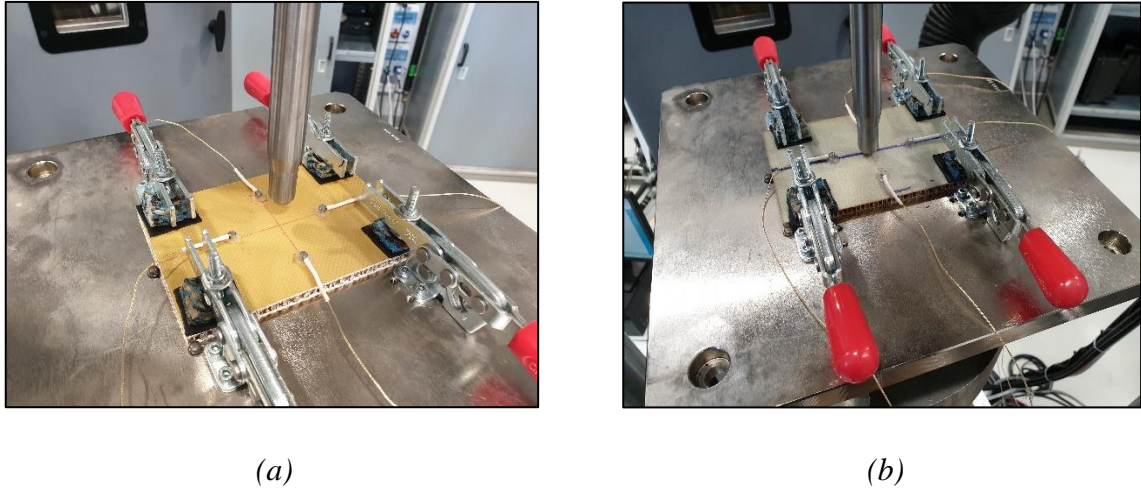


Figure 39. Piezo electric acoustic emission sensors placement on the specimens: a) Aramid sandwich panel, b) E-glass sandwich panel.

4.3 Quasi-Static Test Results and Discussion

The damage mechanisms within the constituent of the sandwich panel (i.e., the face sheet and core structure) are investigated under the quasi-static indentation loading configuration. Figure 40 presents representative load versus deflection curves for sandwich panels with the E-glass and aramid face sheets. For the aramid sandwich panel specimen, the second sharp drop in the indentation load, taking place at the deflection of 8.76 mm, is associated with the damage formation in the upper face sheet. As the test continues, the core structure and bottom face sheet start carrying the applied load. Subsequently, the core is completely crushed thereby leading to the second drastic drop in the load level. The bottom face sheet carries the load until sandwich panel is fully penetrated by the indenter at the load and the displacement levels of 3624 N and 15.9 mm, respectively. As for the sandwich panel with the E-glass face sheet, the upper face sheet is entirely damaged at about the load and deflection values of 1634 N and 6.08 mm, which corresponds to the first drop in the graph. As in the case of the aramid sandwich

panel, the lower face sheet and core structure embrace the indentation load as the test progresses until the core structure is totally crushed where the load level drops down to the value of 1125 N. The second larger drop in the load level occurs at the load and deflection values of 2702 N and 13.2 mm deflection, indicating the onset of complete deformation and penetration of the core and the bottom face sheet. Considering the areas under the load-deflection graphs of the E-glass and aramid sandwich panels, it can be concluded that the aramid panel has a better energy absorbing capability. Additionally, Figure 41 (a) and (b) indicate that the aramid panel is deformed in a non-localized manner under the indentation load and thus withstands a higher load level through distributing the indentation energy across panel geometry. On the other hand, due to the brittle nature of the E-glass fiber with respect to the aramid one, the upper E-glass face sheet fails at lower load level and the induced damage is rather localized as can be seen from Figure 42 (a) and (b). The comparison on the slope of the load versus deflection curve for E-glass and aramid sandwich panels also indicates the brittle nature of the E-glass panel face sheet under the indentation loading.

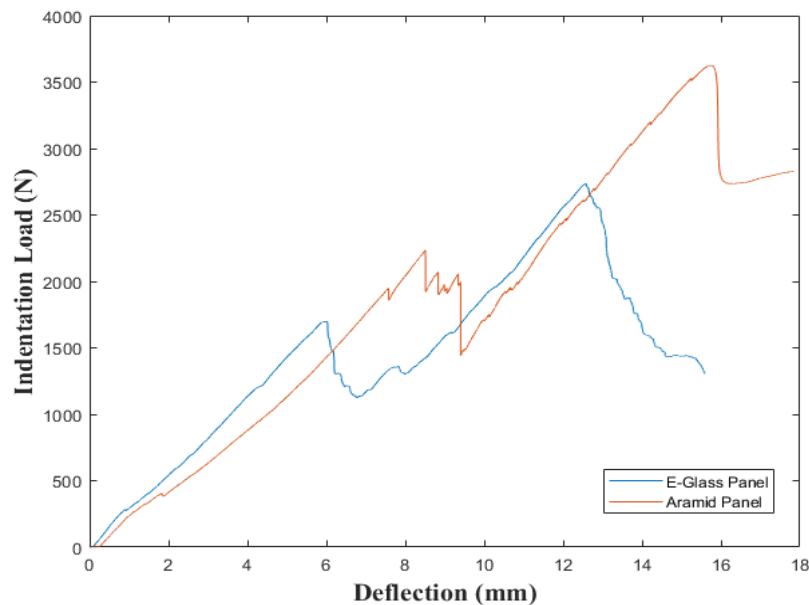


Figure 40. Quasi-static indentation test load and deflection results.

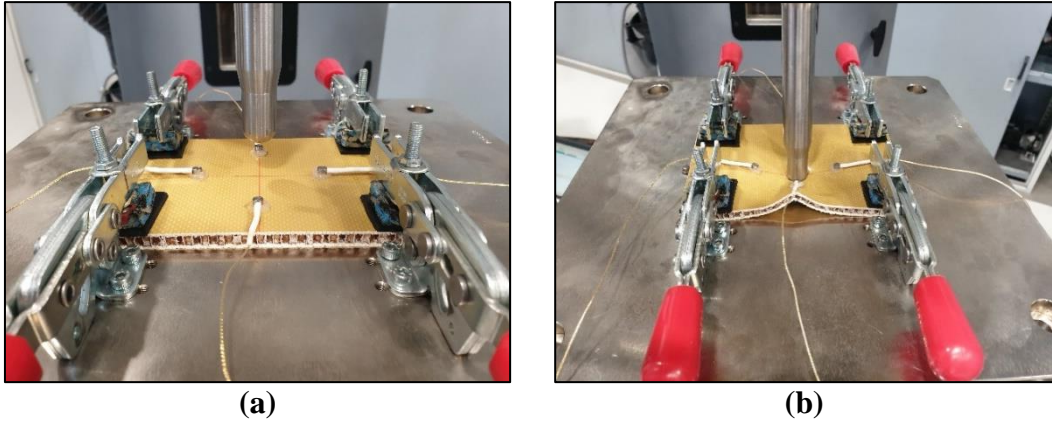


Figure 41. Aramid sandwich panel before (a) and after (b) the indentation test.

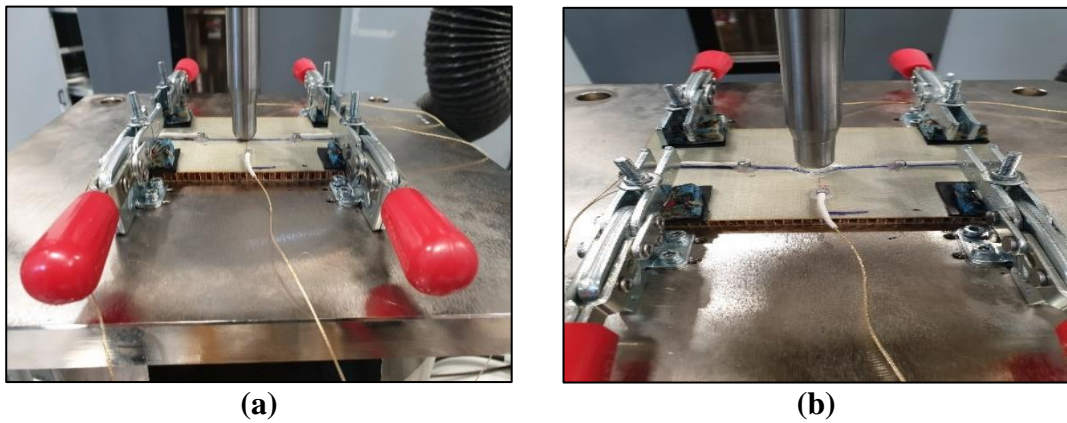


Figure 42. E-glass sandwich panel before (a) and after (b) the indentation test.

4.4 Acoustic Emission Results and Clustering

Clustering was performed based on the acoustic emission count and weighted peak frequency which are determined for each hit point of the acoustic emission data acquired during the indentation test. Acoustic emission counts represent the number of times that the signal amplitude exceeds a specified threshold. The waveform data in the time domain is converted to the frequency domain by applying Fast Fourier Transform (FFT). As can be seen in Eq.16, the weighted peak frequency (WPF) is a function that depends on the frequency centroid ($f_{centroid}$) and the peak frequency of the hit. The frequency centroid ($f_{centroid}$) is considered as the center of mass of the frequency spectrum while the peak frequency (f_{peak}) is the maximum frequency value in the frequency domain of a waveform. The frequency centroid can be obtained through a weighted mean formula as given in Eq.17 where $M(s)$ is the magnitude of each frequency (s).

$$WPF = \sqrt{f_{centroid} \times f_{peak}} \quad (16)$$

$$f_{centroid} = \sum_{s=0}^{s=1000} f(s)M(s) / \sum_{s=0}^{s=1000} M(s) \quad (17)$$

Clustering is performed using the k-means algorithm with the Euclid distance parameter by using the Elki software. Given the fact that k-means clustering approach is an unsupervised method, and hence does not define any preset number of possible clusters. In order to specify an optimum cluster number by using hit points in the acoustic emission data, *GAP* function method is used which is frequently preferred approach in k-means clustering algorithms as seen in Figure 44 and Figure 45. Thanks to this function, an error value (w_k) is found for different cluster numbers used in the clustering algorithm. The number of clusters that maximize the *GAP* function computed based on the input data is considered the most accurate number of clusters for the entire data set. *GAP* function is defined as in Equation 18;

$$GAP_n(k) = E_n^*\{\log(\omega_k)\} - \log(\omega_k) \quad (18)$$

where n denotes the size of a hit-based sample points data, k is the number of the clusters which are evaluated. By using the Monte Carlo method, $E_n^*\{\log(\omega_k)\}$ is the expectations which are calculated from the sample points [62].

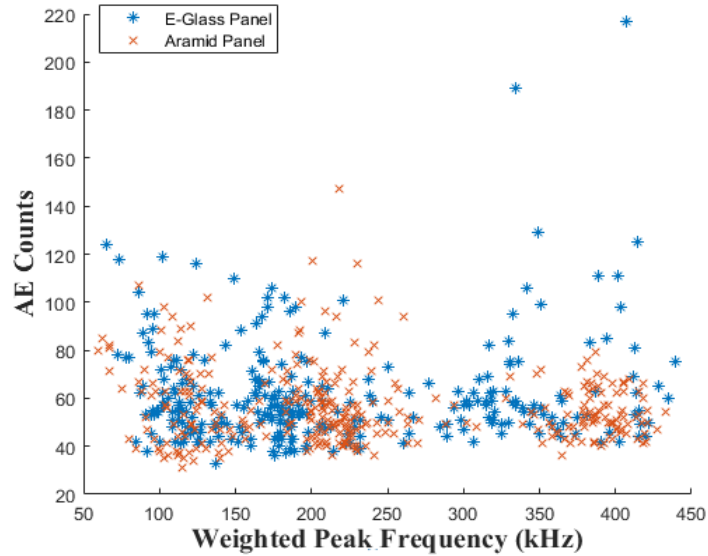


Figure 43. AE counts versus weighted peak frequency plot of aramid and E-glass samples.

The graph of the filtered acoustic emission data obtained from the samples as a result of quasi-static indentation tests is shown in Figure 43. This plot represents the hit data before the implementation of the clustering algorithm. For correct clustering of the acoustic emission data, the estimation of the initial clustering coefficient in the k-means algorithm is very important.

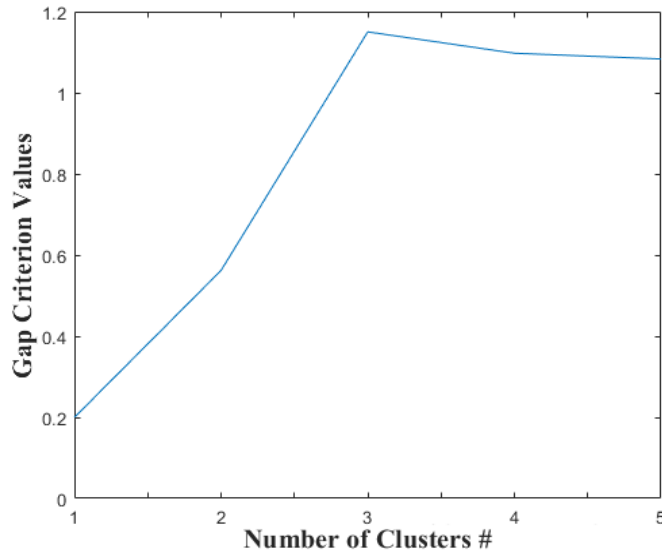


Figure 44. Aramid panel GAP values of calculated for each cluster.

Figure 44 and Figure 45 show the *GAP* values of sandwich panels obtained from the function. Composite sandwich panels have various failure mechanisms such as matrix cracking, fiber breakage, and the delamination of face sheet plies, fiber-matrix debonding and core crushing. In this case, *GAP* function is evaluated for five main different clusters. The *GAP* analysis has generated respectively three and four clusters for aramid and E-glass as an optimum number for k-means algorithm clustering. This means that when the acoustic emission data is classified with three and four clusters, the best separation of the data points is achieved thereby representing the most dominant damages on the samples.

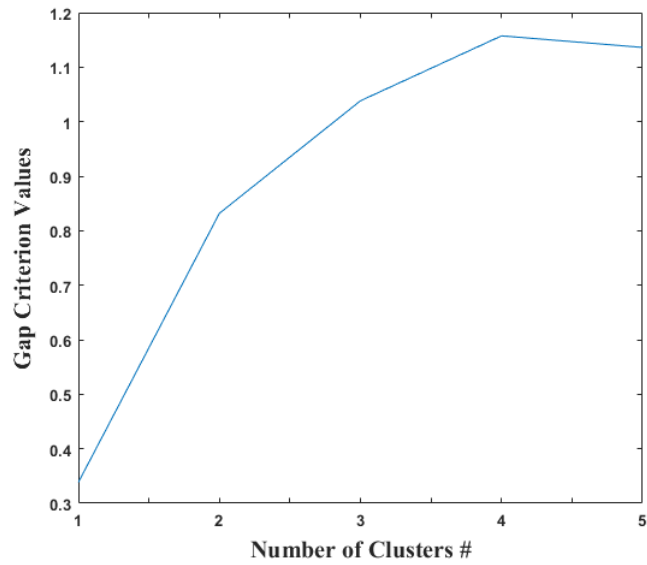


Figure 45. E-glass panel GAP values of calculated for each cluster.

For aramid sandwich panel, figure 46 shows three distinctive clusters with their center of mass located at the weighted peak frequencies of 110, 215 and 390 kHz. The fact that the center of mass of each cluster is distinctly far from each other bespeaks the effective clustering of the acoustic emission data.

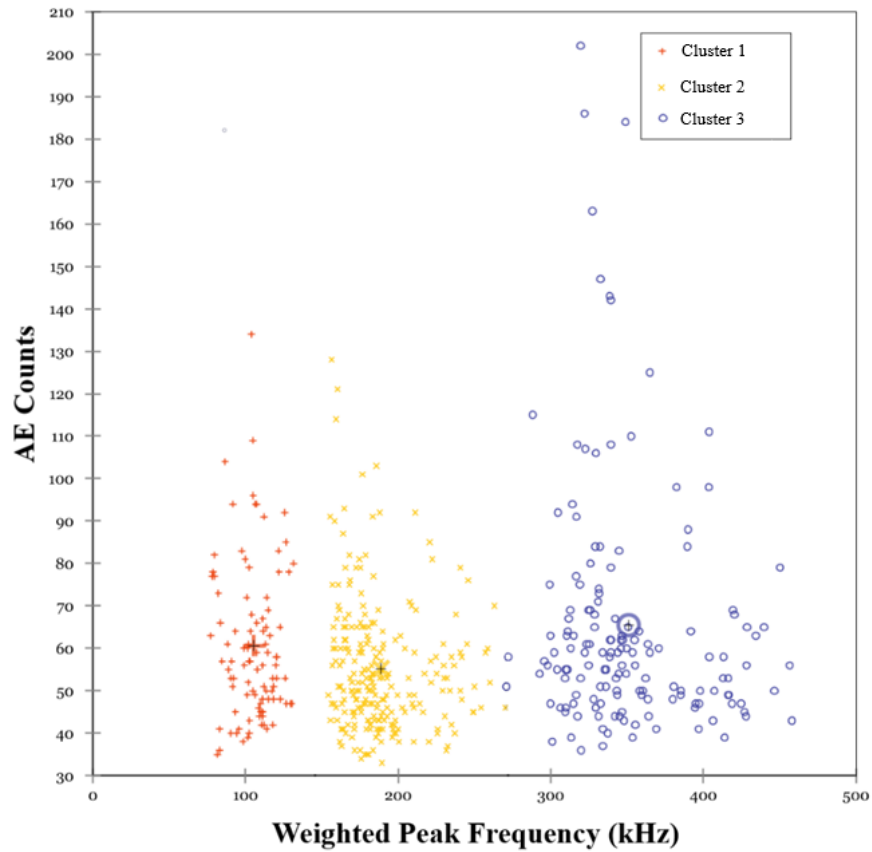


Figure 46. Acoustic emission vs weighted peak frequency graph of aramid panels in terms of k-means algorithm clusters.

Acoustic emission cumulative energy is used to be able to assign each cluster to a specific damage type. To this end, we have plotted the applied indentation load, and cumulative AE energy for each cluster versus time (recording time of the waveforms) for the aramid panel in Figure 47. The cumulative acoustic emission energy of each cluster is calculated separately as a function of time through summation over acoustic emission energy of each hit point in the corresponding cluster. The comparison of the load versus time and the cumulative AE energy versus time graphs enables one to associate a given damage type to a cluster. Figure 47 is divided into four different stages. In the stage I, the panel experiences elastic deformation until the minuscule kink due to the first damage induced by the tip of the hemispherical indenter. The load versus time plot in this region is of a slightly concave nature as also reported in the literature. Moreover, this region is almost devoid of acoustic emission activity pointing to the fact that there is no significant

amount of damage formation in the panel. This can also be inferred from the lack of any noticeable drop in the applied load as a function of time.

As for the second stage, the load curve acquires a convex shape deviating from the linearity indicating the formation of damage in the panel. The convex curve might be attributed to the consolidation/compaction of the core due to the crushing of the cell walls. Correspondingly, the cluster 1 goes through a sudden upsurge and then remains almost constant, thus implying that the cluster 1 is related to the AE activities originating from core compaction or crushing. Towards the end of the second stage, the load curve experiences two obvious drops pointing out to a notable damage development in the face sheet material. These two drops are in coincidence with the jumps in the cumulative AE energy corresponding to the cluster 2 in Figure 47. As such, the cluster 2 can be prudently associated with the matrix cracking failure mechanism in the upper face sheet. This argument can also be corroborated referring to the findings of literature such that AE counts with the weighted peak frequency range of 180-260 Hz have been reported to belong to matrix cracking [64].

At the beginning of the third stage, the indenter has already penetrated the upper face sheet completely and hence starts inflicting damage within the core. Therefore, the cumulative AE energy of the matrix cracking damage type (cluster 2) remains nearly constant within the third stage. Also note that the cumulative AE energy of cluster 1, already associated with the core material, reveals a mild uplift, which is being an evidence of the fact that the core has been penetrated and gradually damaged by the indenter. At the end of the third stage, the cumulative AE energy of matrix cracking (cluster 2) indicates a sudden jump, which corresponds to a large drop in the load level therein. This sharp rise in the cumulative AE energy of cluster 2 can be contributed by damage formation in the matrix of the bottom face sheet as well as in the phenolic resin used to impregnate Nomex paper in the core material.

In the stage IV, the cumulative AE energy for matrix cracking keeps increasing due to the damage formation in the matrix of the bottom face sheet and phenolic resin of

Nomex paper in the core material. Additionally, given the fact that in the stage IV, the core material is being crushed further through shearing of the cell walls, cumulative AE energy for the cluster 1 continuously increases in this region, further confirming our assignment of the cluster 1 to the core crushing damage type. Having attributed the cluster 1 and 2 to core crushing and matrix cracking, respectively, it is meaningful to associate the cluster 3 with the fiber breakage. In the stage II, it is realizable that the magnitude of the cumulative AE energy has the highest, intermediate and lowest values for core, matrix and the fiber. This is due to the fact that the stiffer constituent gives rise to high-frequency waveform with a small amplitude. In the stage IV, the magnitude of the cumulative AE energy of the core falls below the matrix, which might be an indication that there is a stiffening on the cell walls due to the core crushing.

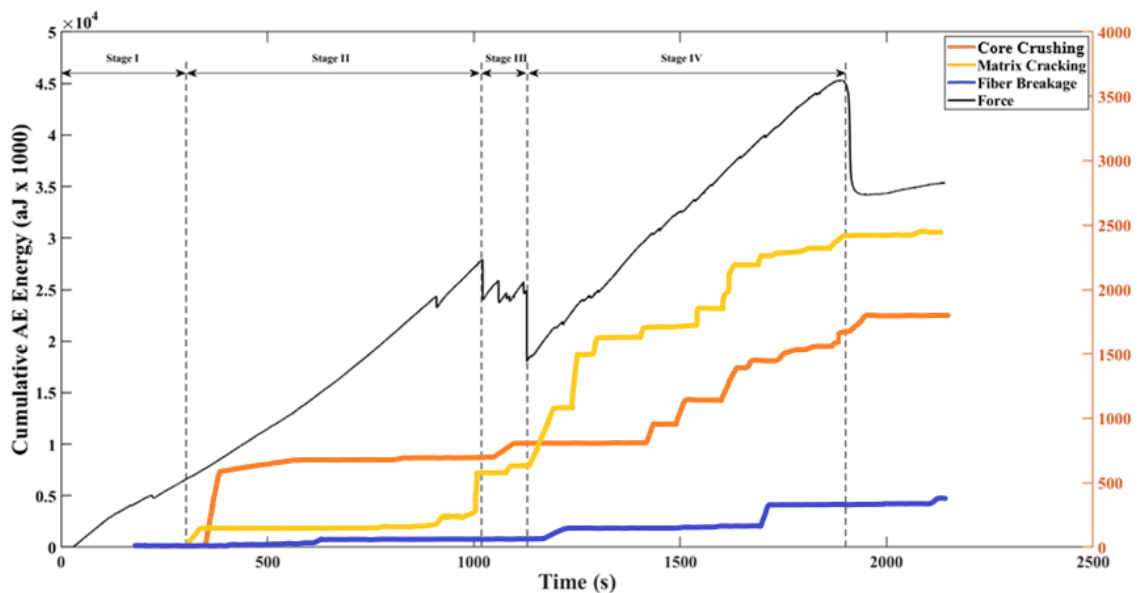


Figure 47. The variation of cumulative AE energy and load as a function of time for the aramid panel.

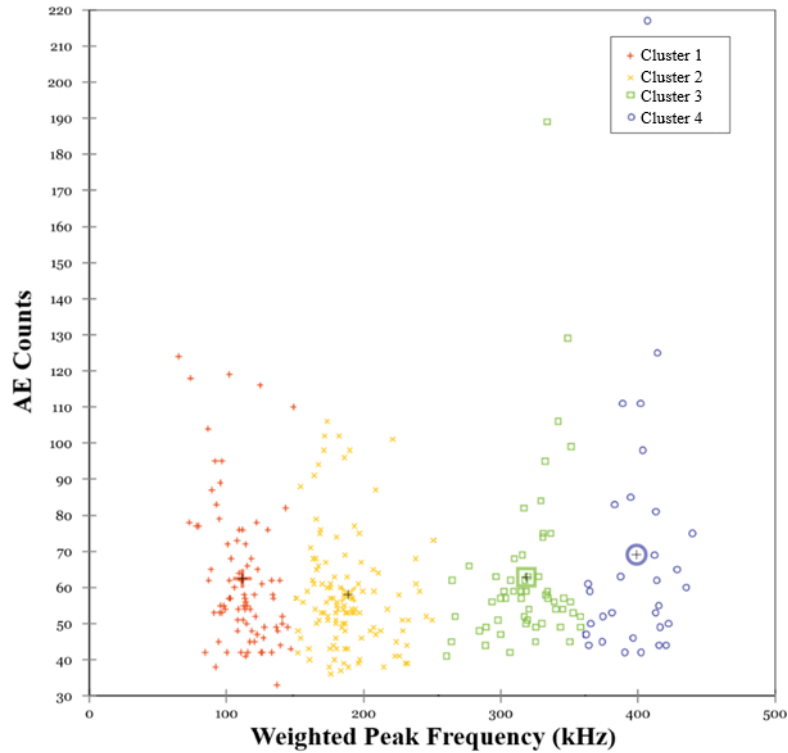


Figure 48. Acoustic emission vs weighted peak frequency graph of E-glass panels clustered with k-means algorithm.

For E-glass sandwich panel, Figure 48 shows the AE counts versus weighted peak frequency values of the four clusters with their center of mass located in the weighted peak frequencies of 115 kHz, 190 kHz, 315 kHz and 400 kHz, respectively. According to the clusters obtained from the AE results, it is seen that unlike the aramid panel, there are four clusters belonging to each distinct damages type. As indicated in the Figure 45, the optimum GAP criterion evaluation is performed for cluster numbers varying between one and five. However, it is seen that the optimum GAP value is maximized for the cluster number of four. Hence, it is concluded that there is four main and dominant damage.

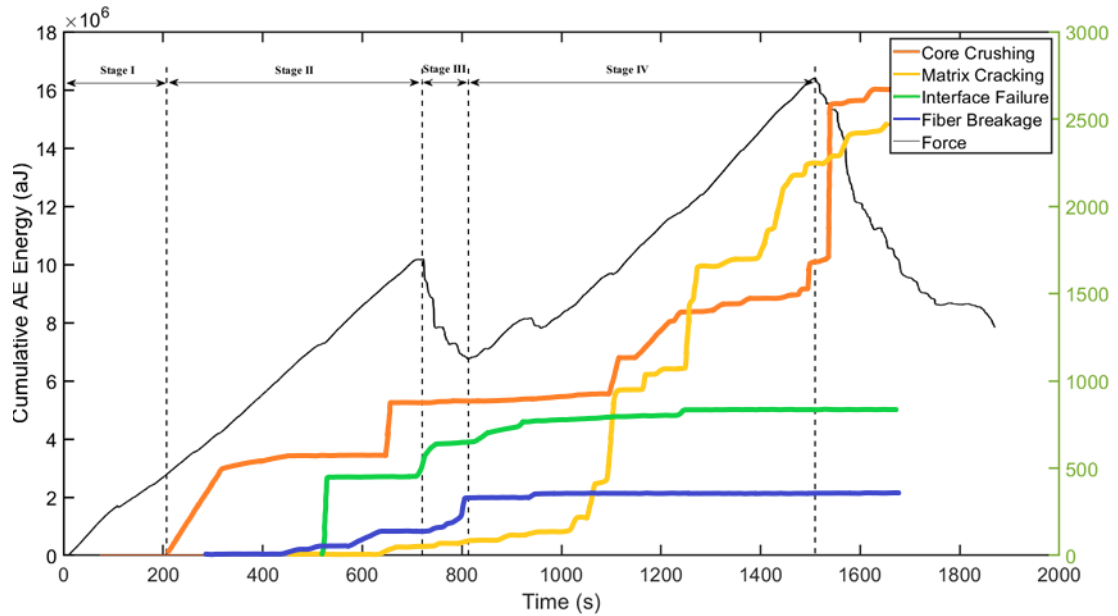


Figure 49. Cumulative AE energy versus Load chart of E-glass panel in time domain.

In Figure 49, the indentation load and cumulative AE energy of each cluster are plotted as a function of time for the E-glass sandwich panel. Knowing that the specimen will show distinct damage formations during the test during which the corresponding cumulative AE energy accumulates, Figure 49 is discussed under the consideration of four different time stages. In the stage I, one can easily realize that the force-displacement curve is identical to the one in Figure 47, which has a negligible fracture kink caused by the hemispherical geometry of the indenter. Additionally, the absence of a significant acoustic emission activity indicates that the specimen undergoes an elastic deformation during this stage.

The load curve acquires a non-linear profile in the stage II where each cluster experiences an abrupt or notable increase in the cumulative AE energy thereby pointing to the fact that various damage types concurrently emerge in the upper face sheet and the core. The core walls are subjected to compaction and crushing due to the transfer of indentation load from the upper face sheet. This is in line with the sudden increase in the cumulative AE energy of the cluster 1 whereby one can reliably associate this cluster to the core crushing or compaction damage in the E-glass sandwich panel. It is noted that

the peak load value of the E-glass panel is lower than that of the aramid panel, thus implying that the partial penetration of the upper face sheet by the indenter occurs earlier for the E-glass panel. This prominent difference might be attributed to the considerable amount of delamination and matrix-fiber debonding damages eventuated in the upper face sheet and in turn, the load-carrying capability of the upper face sheet is decreased. In the light of these evaluations, the instantaneous sharp uptrend in the cumulative AE for the cluster 3 can be associated with the interface damage type. This conclusion is supported by literature findings such that the weighted peak frequency of delamination and fiber-matrix debonding damages typically takes place in the frequency range of 250-300 kHz [80].

At the beginning of the stage III, the upper face sheet is critically cracked, and consequently, the indenter tip makes a point contact with the core thus leading to a drop in load magnitude. The cumulative AE energy of cluster 3 is of a rapidly ascending trend due to the delamination and debonding damage formations within the upper face sheet and this further confirms our assignment of the cluster 3 to the interface damage type. Moreover, within the stage III, the sudden increase in the cumulative AE energy of cluster 4 coincides with the drop of the load to its minimum value, which is attributed to complete penetration of the upper face sheet by the indenter. This observation enables us to infer that the cluster 4 is related to fiber breakage, which is one of the significant damage types in the face sheet. It is also known from the literature that the fiber breakage damage type occurs in the frequency level higher than 400 kHz [81]. It can be concluded in a straightforward manner that interface failure and fiber breakage are dominant damage types induced by the penetration of the upper face sheet. The remaining cluster, namely, the cluster 2 can be expediently attributed to the matrix cracking. Due to the brittle material behavior of E-glass face sheet, permanent deformation occurs only in the area where there is intense indentation load. The cumulative AE energy increase for the matrix cracking is expectedly low at the early stages of the test as there is relatively less damage in other locations of the sandwich panel.

In the stage IV, due to the complete penetration of the upper face sheet, the bottom face sheet and the core structures do carry the load. This explains the monotonic second

increase of the load as a function of time. A substantial increase in the cumulative AE energy of both the cluster 1 (core crushing) and cluster 2 becomes obvious. Gradual advancement of the hemispherical indenter through the core causes core walls to expand and get damaged under the shear force. As a result, the cumulative AE energy of the core crushing keeps increasing and at the end of the stage IV, it reveals a rapid jump due to the complete penetration of the core. Moreover, the gradual rise of cumulative AE for the matrix cracking is contributed by the damage formation in the matrix of the bottom face sheet and the phenolic resin constituent of Nomex paper.

4.5 Scanning Electron Microscopy Analysis of Failed Sandwich Panels

Having tested sandwich panel specimens under indentation loading, the specimens are dissected using a circular diamond saw to expose the fracture surface for microscopic analysis. SEM images of the fracture surface are taken to examine the types of damages along the thickness direction of the panels. Various damage types have been observed across the fracture surface, each of which is elaborated in figures 50-54. Figure 50 and Figure 51, shows damage types in the E-glass face sheet created due to the indentation load such as matrix cracking which triggers the fiber-matrix debonding and fiber pull-out, inferred by the fiber imprints.

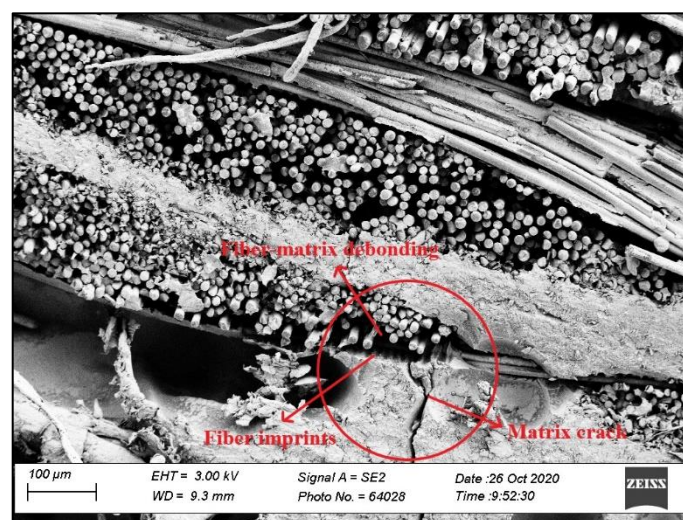


Figure 50. Damage types observed in the face sheet of the E-glass panel.

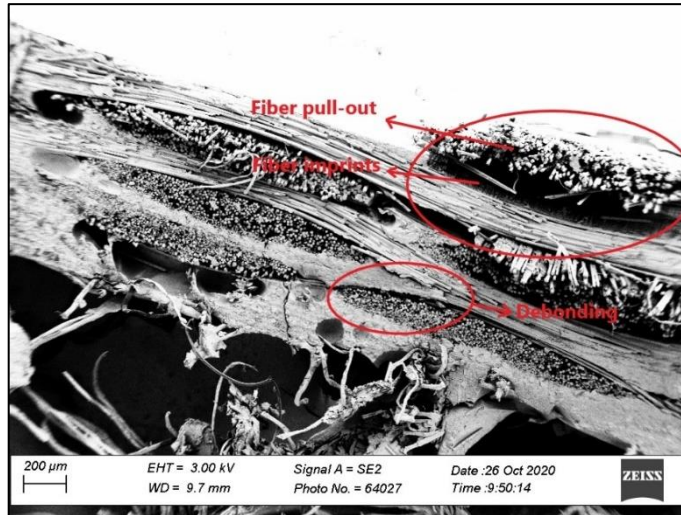


Figure 51. Micrograph of the fiber-pull out damage mechanism observed in the face sheet of the E-glass panel.

Cracking in the matrix of face sheet layers contributes to poor bonding between the fiber and matrix structure. As a result of this, the fiber pull-out damage mechanism occurs which is being an evidence of the fact that the fibers separated from the matrix by dragging left traces on the matrix.

The damage mechanism caused by the separation of the layers in the face sheets of the sandwich panel is named delamination. We can able to make an inference across the literature findings for the strength degradation of the face sheet because of delamination [61]. As a consequence of the damage mechanism that started with the adhesion between the laminated layers consisting of E-glass fibers, a gap was observed between the plies in the microstructure and delamination took place there, as presented in Figure 52 and Figure 53.

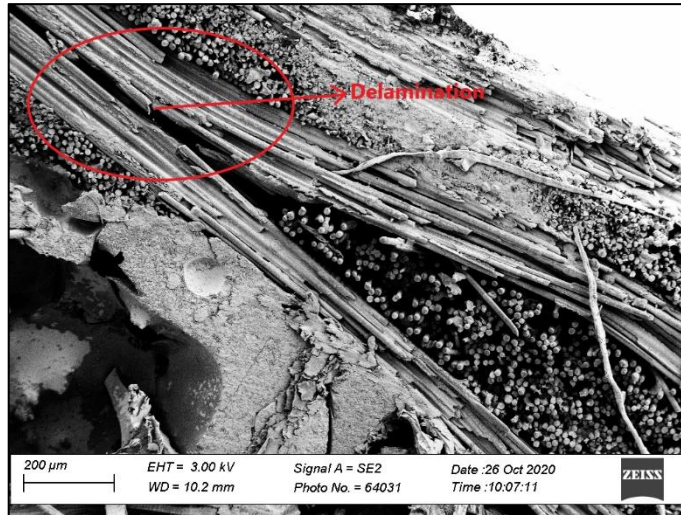


Figure 52. SEM image of the delamination damage mechanism between E-glass face sheet layers.

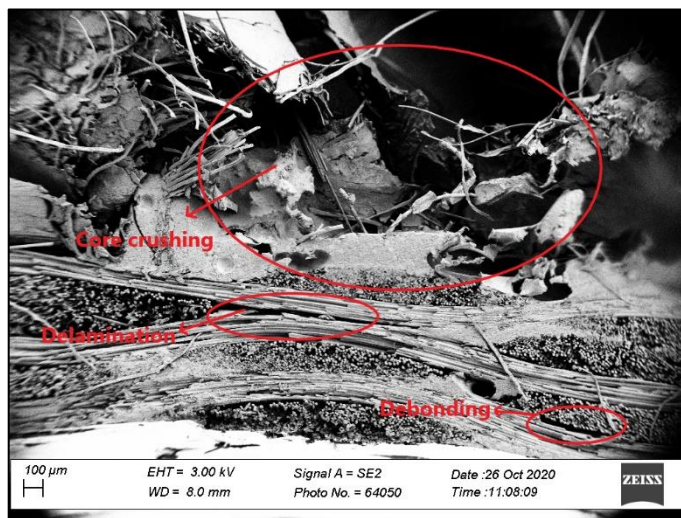


Figure 53. Various face sheet and honeycomb core damage mechanisms existing on the interface of the E-glass panel.

As mentioned in the previous section, growing acoustic emission activity in the third stage of the aramid panel indentation test was observed and these clusters are associated with the core crushing and matrix cracking. Figure 54 shows these damage

formations which are appeared due to the indentation load acting on the bottom face sheet and the core of the aramid panel.

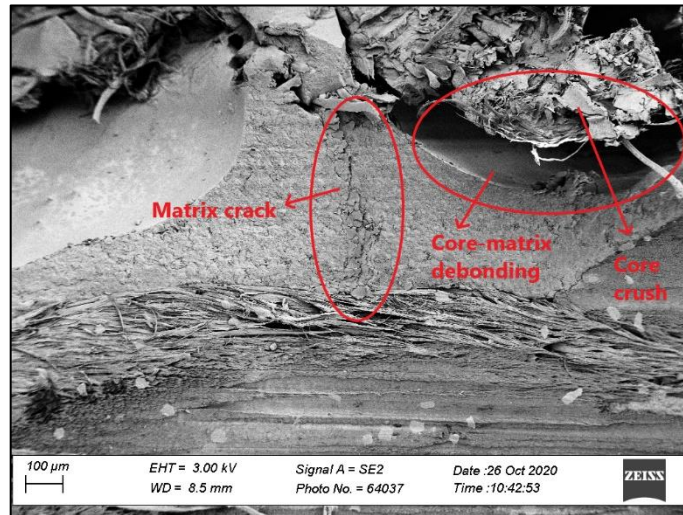


Figure 54. Damage mechanisms of the aramid panel in the microstructure.

CHAPTER 5

5. Conclusion

This thesis investigates the electromagnetic and structural performance of two different flat-shaped radome sandwich panels composed of E-glass and aramid skin and low dielectric constant Nomex honeycomb core. In this context, free space test measurements are conducted on the sandwich panels manufactured with the hot press method as well as their constituents in the frequency range of 5.85-25 kHz to acquire electrical parameters of the samples such as dielectric constant and loss tangent values. For this measurement, a network analyzer with the capability of providing instant reaction to the electromagnetic waves in this frequency range is used. It is found that the aramid and E-glass face sheets have an almost linear dielectric constant versus frequency curve with dielectric constant values of approximately 3.5 and 4.75, respectively. Since the aramid prepreg face sheet material has a lower dielectric coefficient, it can be a suitable insulator skin material for the radome sandwich panel applications. In contrast, the E-glass face sheet has a lower loss tangent value which is another significant electrical parameter for a well insulating radome wall. The measured electrical properties of the face sheets could not provide conclusive results in terms of finding the most appropriate face sheet material for constructing improved electromagnetic transmission performance for the sandwich panel. Therefore, we have also performed free space tests on the sandwich panel. It is important to note that for reliable comparison between two different sandwich panels in terms of their electromagnetic performance, the panels should have identical thicknesses for both face sheets and the core given the fact that the electromagnetic waves have different transmissions and reflections depending on the thickness of the layer they pass through. The results of the free space tests on the sandwich panels indicate that in the frequency range of 5.85-12 kHz, there is no considerable amount of loss difference between E-glass and aramid sandwich panel samples whereas the aramid panel has a substantially superior against the E-glass in terms of transmission loss in the frequency range of 12-25 kHz.

The experimental results in terms of free space transmission loss are also numerically generated by using the multilayer substrate numerical model together with the Planar Green's function solver with an excellent agreement among each other. Considering the low dielectric coefficient of the aramid panel as well as the small amount of transmission loss rates especially at high frequencies, one can prudently conclude that the aramid sandwich panel can be a better radome structure with respect to the E-glass sandwich panel.

In the second part of the thesis, we studied the formation and classification of various damage mechanisms in the aramid and E-glass sandwich panels for radome application under the quasi-static indentation loading by using the acoustic emission method. The results of the indentation mechanical tests indicate that the aramid sandwich panel has a higher energy absorption capacity than the E-glass one. Additionally, the aramid panel deforms in a non-localized manner and thus withstands a higher load level through distributing the indentation energy across panel geometry. As for the AE analysis, *GAP* function method is used for selecting the optimum cluster number, which led to the three and four clusters for the aramid and E-glass panels, respectively. To this end, clustering is performed with the k-means algorithm over 3 clusters for the aramid panel and 4 clusters for the E-glass panel, based on the acoustic emission count and weighted peak frequency. Furthermore, the cumulative AE energy and load values are plotted and analyzed in the time domain in order to associate the damage types with the appropriate clusters. As a result, for the aramid panel, the three clusters with the WPF range of 80-120 kHz, 150-250 kHz, 300-460 kHz are associated respectively with three distinct damage types, namely, core crushing, matrix cracking and fiber breakage. Moreover, there is an additional cluster observed for the E-glass in the WPF range of 260-360 kHz, which is attributed to the interface failure due to the debonding/delamination within the face sheet. SEM analysis of damaged cross-sections of the samples reveals that all failure types identified with the AE method form as a result of the quasi-static indentation test, proving that the AE method can be reliably utilized for the identification of the barely visible damage types for the sandwich panels.

References

1. Russo, O., A. Colasante, G. Bellaveglia, F. Maggio, L. Marcellini, L. Scialino, L. Rolo, J. C. Angevain and R. Midthassel. "State-of-the-art Materials for Ku and Ka Band Mobile Satellite Antenna Radomes Telecommunications Ground Segments Workshop esa/estec, noordwijk, the netherlands 3-5 october 2012." (2012)
2. Dennis Kozakoff, Analysis of Radome Enclosed Antennas, Second Edition , Artech, 2009.
3. R. H. Cary, Avionic Radome Materials, 956. number/AD (United States. National Technical Information Service), 1974
4. Baxter, J. P., Scientists Against Time, Boston, MA: Little, Brown and Company, 1952.
5. Eggleston, W., Scientists at War, Toronto, Canada: Hunter Rose Company, Ltd., 1950
6. Lien Fredrik, Modelling and Test Setup for Sandwich Radomes, Institutt for elektroniske systemer, 2014
7. Baker-Jarvis, J., Jones, C., Riddle, B. et al. Dielectric and magnetic measurements: A survey of nondestructive, quasi-nondestructive, and process-control techniques. Res Nondestr Eval 7, 117–136 (1995). <https://doi.org/10.1007/BF02538826>
8. O. V. Tereshchenko, F. J. K. Buesink and F. B. J. Leferink, "Measurement of complex permittivity of composite materials using waveguide method," 10th International Symposium on Electromagnetic Compatibility, York, 2011, pp. 52-56.
9. 141 A. C. Lynch, "Precise measurements on dielectric and magnetic materials,"IEEE Trans. Insurn. Meas.. vol. 1M-23, pp. 425-430,1974
10. Agilent Basics of Measuring the Dielectric Properties of Materials Agilent Technologies, Inc. 2005, 2006
11. IST 110: Introduction to Information Sciences and Technology Bart Pursel, Ph.D. Penn state university, Recyclable thermoset plastics | IST 110: Introduction to Information Sciences and Technology (psu.edu)
12. <https://romeorim.com/what-are-composites>
13. <http://www.recycledplastic.com/index.html%3Fp=10288.html>

14. Michel Biron, in *Material Selection for Thermoplastic Parts*, 2016
15. <https://www.compositesworld.com/articles/the-fiber>
16. X-Q. Dai, in *Biomechanical Engineering of Textiles and Clothing*, 2006
17. Learning Center - What are Unidirectional Carbon Fiber Fabrics? (fibreglast.com)
18. <https://www.rockwestcomposites.com/blog/anisotropic-vs-isotropic-why-it-matters-in-composites/>
19. "Composites | Composite Materials". Mar-Bal, Inc. 2013-10-15. Retrieved 2020-12-18.
20. Predicting Flexural Strength Of Composite Honeycomb Sandwich Panels Using Mechanical Models Of Face Sheet Compressive Strength, Nick Bruffey William Shiu June, 2016.
21. Research and Development in Modern Materials A school science activity sequence based on research at Deakin's Institute for Frontier Materials Honeycomb Structures | Research and Development in Modern Materials (deakin.edu.au)
22. <http://www.paneltech.biz/photos/honeycomb-corrugated.gif>
23. May 2017IOP Conference Series Materials Science and Engineering 197(1):012046 Follow journal DOI: 10.1088/1757-899X/197/1/012046
24. E. Whalen, G. Gampala, K. Hunter, S. Mishra and C. J. Reddy, "Aircraft Radome Characterization via Multiphysics Simulation," 2018 AMTA Proceedings, Williamsburg, VA, 2018, pp. 1-4.
25. U. Jakobus, "Comparison of Different Techniques for the Treatment of Lossy Dielectric/Magnetic Bodies Within the Method of Moments Formulation," *AEU International Journal of Electronics and Communications*, Vol. 54, No. 3, January 2000, pp. 163–173.
26. Altair Feko User Guide, <https://www.altairuniversity.com/wp-content/uploads/2015/03/UserManual.pdf>
27. Overview of Acoustic Emission Testing (AET), <https://inspectioneering.com/tag/acoustic+emission>
28. Pashmforoush, Farzad & Khamedi, Ramin & Fotouhi, Mohammad & Hajikhani, Milad & Ahmadi Najafabadi, Mehdi. (2014). Damage Classification of Sandwich Composites Using Acoustic Emission Technique and k-means

- Genetic Algorithm. *Journal of Nondestructive Evaluation*. 33. 10.1007/s10921-014-0243-y.
29. Pagano, N.J., Schoeppner, G.A.: Delamination of polymer matrix composites: problems and assessment. In: Kelly, A., Zweben, C. (eds.) *Comprehensive Composite Materials*, pp. 433–528. Elsevier Science, Oxford (2000)
 30. Khamedi, R., Fallahi, A., Refahi Oskouei, A.: Effect of martensite phase volume fraction on acoustic emission signals using wavelet packet analysis during tensile loading of dual phase steels. *Mater. Des.* 31(6), 2752–2759 (2010)
 31. Uenoya, T.: Acoustic emission analysis on interfacial fracture of laminated fabric polymer matrix composites. *J. Acous. Emiss.* 13, 95–102 (1995)
 32. Davis, J.R.: *ASM Handbook. Non-destructive evaluation and quality control*. ASM International, Materials Park, OH (1994)
 33. Ely, T.M., Hill, E.K.: Longitudinal splitting and fibre breakage characterization in graphite/epoxy using acoustic emission data. *Mater. Eval.* 53(2), 288–294 (1995)
 34. Uenoya, T.: Acoustic emission analysis on interfacial fracture of laminated fabric polymer matrix composites. *J. Acous. Emiss.* 13, 95–102 (1995)
 35. Morsher, G.N., Fernandez, J.M., Purdy, M.J.: Determination of interfacial properties using a single-fiber microcomposite test. *J. Amer. Ceram. Soc.* 79(4), 1083–1091 (1996)
 36. Ativitavas, N., Fowler, T., Pothisiri, T.: Acoustic emission characteristics of pultruded fiber reinforced plastics under uniaxial tensile stress. In: *Proceedings of European WG on AE*, pp. 447-454. Berlin, (2004)
 37. Kenji, K., Ono, K.: Pattern recognition of acoustic emission signals from carbon fiber/epoxy composites. In: *Proceedings of the 7th international acoustic emission symposium (IAES)*, Zaragoza, 1987
 38. Yan, T., Holford, K., Carter, D., Brandon, J.: Classification of acoustic emission signatures using a self-organization neural network. *J. Acous. Emiss.* 17(1/2), 49–59 (1999)
 39. Philippidis, T.P., Nikolaidis, V.N., Anastassopoulos, A.A.: Damage characterization of carbon/carbon laminates using neural networks techniques on AE signals. *NDT & E Int.* 31(5), 329–340 (1998)
 40. Godin, N., Huguet, S., Gaeertner, R.: Integration of the Kohonen's self-organizing map and k-means algorithm for the segmentation of the AE data

- collected during tensile tests on cross-ply composites. *NDT & E Int.* 38(4), 299–309 (2005)
41. Ni, Q.Q., Iwamoto, M.: Wavelet transform of acoustic emission signals in failure of model composites. *Eng. Fract. Mech.* 69(6), 717–728 (2002)
 42. Marec, A., Thomas, J.H., Guerjouma, E.R.: Damage characterization of polymer-based composite materials: multivariable analysis and wavelet transform for clustering acoustic emission data. *Mech. Sys. Sig. Proc.* 22(6), 1441–1464 (2008)
 43. Quispitupa, A., Shafiq, B., Just, F., Serrano, D.: Acoustic emission based tensile characteristics of sandwich composites. *Compos. B* 35, 563–571 (2004)
 44. C. Visconti, I., Teti, R.: Acoustic emission from composite materials. (1979)
 45. Sachse, W., Yamaguchi, K., Roget, J.: Acoustic emission: current practice and future directions. Presented at the (1991)
 46. Jensen, L.F., Hansen, M.M., Pertoldi, C., Holdensgaard, G., Mensberg, K.-L.D., Loeschcke, V.: Local adaptation in brown trout early life-history traits: implications for climate change adaptability. *Proceedings of the Royal Society B: Biological Sciences.* 275, 2859–2868 (2008)
 47. Higo, Y., Inaba, H.: The general problems of AE sensors. In: *Acoustic Emission: Current practice and future directions.* ASTM International (1991)
 48. Hellier, C.J.: Radiographic testing. *Handbook of Non-destructive Evaluation,* McGraw-Hill, New York, NY. (2001)
 49. Unnþórsson, R.: Hit detection and determination in AE bursts. In: *Acoustic Emission-Research and Applications.* IntechOpen (2013)
 50. Hamstad, M.A.: Acoustic Emission Primer, Lecture delivered by Dr. Hamstad at the acoustic emission working group meeting on august 4, 2003 (aewg-46). internet, 2004
 51. Shull, P.J.: *Nondestructive evaluation: theory, techniques, and applications.* CRC press (2002)
 52. Prosser, W.H.: *Advanced AE techniques in composite materials research.* (1996)
 53. Prosser, W.H.: *Waveform analysis of AE in composites.* (1998)
 54. Tsamtsakis, D., Wevers, M., De Meester, P.: Acoustic emission from cfrp laminates during fatigue loading. *Journal of reinforced plastics and composites.* 17, 1185–1201 (1998)

55. Bhat, M.R., Majeed, M.A., Murthy, C.R.L.: Characterization of fatigue damage in unidirectional GFRP composites through acoustic emission signal analysis. *NDT & E International*. 27, 27–32 (1994)
56. De Groot, P.J., Wijnen, P.A.M., Janssen, R.B.F.: Real-time frequency determination of acoustic emission for different fracture mechanisms in carbon/epoxy composites. *Composites Science and Technology*. 55, 405–412 (1995)
57. Nair, Raveendranath & Jha, Rakesh. (2014). Electromagnetic Design and Performance Analysis of Airborne Radomes: Trends and Perspectives [Antenna Applications Corner]. *Antennas and Propagation Magazine, IEEE*. 56. 276-298. 10.1109/MAP.2014.6931715.
58. Panda, Prasanta & Sahoo, Benudhar. (2013). Synthesis and Applications of Electrospun Nanofibers - A Review.
59. Fotouhi, Mohamad, Milad Saeedifar, Seyedali Sadeghi, Mehdi Ahmadi Najafabadi, and Giangiacomo Minak. "Investigation of the Damage Mechanisms for Mode I Delamination Growth in Foam Core Sandwich Composites Using Acoustic Emission." *Structural Health Monitoring* 14, no. 3 (May 2015): 265–80. <https://doi.org/10.1177/1475921714568403>.
60. Mahdian A, Yousefi J, Nazmdar M, Zarif Karimi N, Ahmadi M, Minak G. Damage evaluation of laminated composites under low-velocity impact tests using acoustic emission method. *Journal of Composite Materials*. 2017;51(4):479-490. doi:10.1177/0021998316648228
61. Cantwell, W.J.; Morton, J. (1991). "The impact resistance of composite materials — a review". *Composites*. 22 (5): 347–362. doi:10.1016/0010-4361(91)90549-V
62. Tibshirani, R., Walther, G., Hastie, T.: Estimating the number of clusters in a data set via the gap statistic. *Journal of the Royal Statistical Society: Series B (Statistical Methodology)*. 63, 411–423 (2001)
63. Eisenberg, David, "Evaluation of Quasi-Static Indentation Damage in Aluminum Honeycomb Core - Graphite/Epoxy Sandwich Structures" (2010). Syracuse University Honors Program Capstone Projects. 360.
64. Yilmaz, C., Akalin, C., Gunal, I., Celik, H., Buyuk, M., Suleman, A., Yildiz, M.: A hybrid damage assessment for E-and S-glass reinforced laminated composite

- structures under in-plane shear loading. *Composite Structures*. 186, 347–354 (2018). doi:<https://doi.org/10.1016/j.compstruct.2017.12.023>
65. D. Oplinger and J. Slepetz, "Impact Damage Tolerance of Graphite/Epoxy Sandwich Panels," in *Foreign Object Impact Damage To Composites*, ed. L. Greszczuk (West Conshohocken, PA: ASTM International, 1975), 30-48. <https://doi.org/10.1520/STP33149S>
 66. Sadeghnejad, Soroush & Taraz Jamshidi, Youssef & Sadighi, Mojtaba. (2018). On the Low-Velocity Impact and Quasi-Static Indentation Studies of Nomex™ Honeycomb Composite Sandwich Panels.
 67. <https://romeorim.com/what-are-composites/>
 68. <http://www.modorplastics.com/thermoset-vs-thermoplastics>
 69. Maria Cristina Tanzi, Gabriele Candiaini, in *Foundations of Biomaterials Engineering, 2019*
 70. <https://www.rockwestcomposites.com/blog/anisotropic-vs-isotropic-why-it-matters-in-composites/>
 71. "Composites – Composite Materials" Mar-Bal, Inc. 2013-10-15. Retrieved 2020-12-18
 72. Predicting Flexural Strength of Composite Honeycomb Sandwich Panels Using Mechanical Models of Face Sheet Compressive Strength, Nick Bruffey William Shiu June, 2016.
 73. Research and Development in Modern Materials, Honeycomb Structures, Research and Development in Modern Materials (deakin.edu.au)
 74. <http://www.paneltech.biz/photos/honeycomb-corrugated.gif>
 75. Ultra High Resolution FE-SEM for Versatile Analytics, SUPRA series, 2019
 76. Center, N. resource: Introduction to Acoustic Emission Testing, https://www.nde-ed.org/EducationResources/CommunityCollege/OtherMethods/AE/AE_Intro.htm
 77. Jensen, L.F., Hansen, M.M., Pertoldi, C., Holdensgaard, G., Mensberg, K.-L.D., Loeschke, V.: Local adaptation in brown trout early life-history traits: implications for climate change adaptability. *Proceedings of the Royal Society B: Biological Sciences*. 275, 2859–2868 (2008)
 78. Wu, X.-F.; Zholobko, O. Experimental Study of the Probabilistic Fatigue Residual Strength of a Carbon Fiber-Reinforced Polymer Matrix Composite. *J. Compos. Sci.* 2020, 4, 173. <https://doi.org/10.3390/jcs4040173>

79. <https://www.emlabs.jp/en/1-5-freespace.php>
80. De Groot PJ, Wijnen PAM, Janssen RBF. Real-time frequency determination of acoustic emission for different fracture mechanisms in carbon/epoxy composites. *Compos Sci Technol* 1995; 55: 405-12.
81. Gutkin R, Green CJ, Vangrattanachai S, Pinho ST, Robinson P, Curtis PT. On acoustic emission for failure investigation in CFRP: Pattern recognition and peak frequency analyses. *Mech Syst Sig Process* 2011; 25: 1393–407.
82. <https://composite.kordsa.com/en/images/pdf/product/EF12.pdf>